

AFIP–7 Post-irradiation Examination Summary Report

A. B. Robinson
W. J. Williams
F. J. Rice
B. H. Rabin
D. M. Wachs
M.J. Bybee
N.J. Lybeck

December 2016



The INL is a U.S. Department of Energy National Laboratory
operated by Battelle Energy Alliance

DISCLAIMER

This information was prepared as an account of work sponsored by an agency of the U.S. Government. Neither the U.S. Government nor any agency thereof, nor any of their employees, makes any warranty, expressed or implied, or assumes any legal liability or responsibility for the accuracy, completeness, or usefulness, of any information, apparatus, product, or process disclosed, or represents that its use would not infringe privately owned rights. References herein to any specific commercial product, process, or service by trade name, trade mark, manufacturer, or otherwise, does not necessarily constitute or imply its endorsement, recommendation, or favoring by the U.S. Government or any agency thereof. The views and opinions of authors expressed herein do not necessarily state or reflect those of the U.S. Government or any agency thereof.

AFIP-7 Post-irradiation Examination Summary Report

**A. B. Robinson
W. J. Williams
F. J. Rice
B. H. Rabin
D. M. Wachs
M.J. Bybee
N.J. Lybeck**

December 2016

**Idaho National Laboratory
Idaho Falls, Idaho 83415**

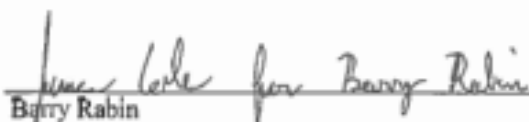
<http://www.inl.gov>

AFIP-7 Post-irradiation Examination Summary Report

INL/RPT-24-40781
Revision 0

December 2016

Approved by:


Barry Rabin
National Technical Lead, USHPRR Fuel Development

12-21-2016
Date


Adam Robinson
Post Irradiation Examination Principal Investigator

12-21-2016
Date

ABSTRACT

The following report contains the results and conclusions from post-irradiation examinations performed on the fuel plates irradiated as part of the AFIP-7 experiment, the first test of base monolithic fuel in a fuel assembly consisting of curved, constrained fuel plates. These examinations include visual examination; eddy-current testing to measure oxide growth; profilometry to measure dimensional changes of the fuel plates; neutron radiography for evaluating fuel condition prior to sectioning; gamma scanning to provide relative measurements of burn-up and indication of fission-product relocation; analytical chemistry to benchmark the physics burn-up calculations; metallographic examination to identify microstructural changes in the fuel, interlayer and cladding; and blister threshold testing. These characterization activities were conducted to demonstrate that the fuel meets irradiation performance requirements for mechanical integrity, geometric stability, and stable and predictable behavior.

CONTENTS

ABSTRACT.....	v
ACRONYMS.....	xi
1. INTRODUCTION AND EXPERIMENT DESCRIPTION	1
2. IRRADIATION HISTORY.....	4
3. NON DESTRUCTIVE POST IRRADIATION EXAMINATION RESULTS.....	8
3.1 Disassembly and Fixturing.....	8
3.2 Visual Examination.....	10
3.3 Neutron Radiography.....	13
3.4 Gamma Scanning	15
3.5 Profilometry and Eddy Current.....	17
4. DESTRUCTIVE POST IRRADIATION EXAMINATION RESULTS	21
4.1 Metallography	21
4.1.1 Plate ZH2	21
4.1.2 Plate ZH4	25
4.2 Chemical Burn-up Analysis	31
4.3 Blister Threshold Testing.....	31
5. DISCUSSION.....	37
6. CONCLUSIONS	48
7. REFERENCES	49

FIGURES

Figure 1. Isometric view of the AFIP-7 element. ⁶	1
Figure 2. AFIP-7 Plate Drawing.....	2
Figure 3. AFIP-7 Nominal Fuel Plate Cross Section.	2
Figure 4. MCNP model X-Y view of the AFIP-7 test assembly.....	4
Figure 5. Hourly constrained lobe power history for cycles 149B (left) and 150B (right).....	5
Figure 6. Fuel plate surface heat flux during irradiation.....	5
Figure 7. MCNP calculated longitudinal end of life fission densities.	6
Figure 8. MCNP calculated fission density distributions for each fuel plate.....	7
Figure 9. AFIP-7 dummy element in milling fixture.	9
Figure 10. Machining the spacer comb from the fuel element.	9
Figure 11. Machining end block material from the AFIP-7 element.	9

Figure 12. Visual examination montage of plate faces ZH1 through ZH4 (left to right).	11
Figure 13. Visual examination image from ZH3.	12
Figure 14. Visual examination image from the bottom of ZH4.....	13
Figure 15. Thermal Radiographs of AFIP-7 ZH1 from top to bottom.	14
Figure 16. Epithermal Radiographs of AFIP-7 ZH1 from top to bottom.....	15
Figure 17. Longitudinal gamma scan profiles.	16
Figure 18. CS-137 transverse gamma scan profile for all plates.	17
Figure 19. BONA4INL USHPRR Plate Checker prior to installation into HFEF.....	18
Figure 20. Thickness profiles for ZH1 (top) through ZH4 (bottom).	18
Figure 21. Eddy current results from ZH1.....	19
Figure 22. Eddy current results from ZH2.....	19
Figure 23. Eddy current results from ZH3.....	20
Figure 24. Eddy current results from ZH4.....	20
Figure 25. AFIP-7 Sectioning Diagram.	21
Figure 26. Metallography image from top edge of fuel zone. Fission density $\sim 1.5\text{E}+21$ fissions/cm ³	22
Figure 27. Metallography image from top edge of fuel zone. Fission density $\sim 1.5\text{E}+21$ fissions/cm ³	22
Figure 28. Metallography image from fuel centerline. Fission density $\sim 2.7\text{E}+21$ fissions/cm ³	22
Figure 29. Metallography image from fuel centerline. Fission density $\sim 2.7\text{E}+21$ fissions/cm ³	22
Figure 30. Metallography image 7 cm from bottom of fuel zone. Fission density $\sim 2.0\text{E}+21$ fissions/cm ³	22
Figure 31. Metallography image 7 cm from bottom of fuel zone. Fission density $\sim 2.0\text{E}+21$ fissions/cm ³	22
Figure 32. Metallography image 7 cm from bottom of fuel zone. Fission density $\sim 2.0\text{E}+21$ fissions/cm ³	23
Figure 33. Cross section from bottom edge of fuel zone. Fission density $\sim 2.0\text{E}+21$ fissions/cm ³	23
Figure 34. High magnification of ZH2 foil edge at top of fuel zone. Fission density $\sim 1.5\text{E}+21$ fissions/cm ³	23
Figure 35. High magnification image of U-Mo/Zr/Al interface at plate midline. Fission density $\sim 2.7\text{E}+21$ fissions/cm ³	24
Figure 36. Image of oxide layer on plate ZH2 at plate mid line.	24
Figure 37. Image of ZH2 foil end at bottom of fuel zone. Fission density $\sim 2.0\text{E}+21$ fissions/cm ³	25
Figure 38. Image of region with thin zirconium diffusion barrier. Fission density $\sim 2.0\text{E}+21$ fissions/cm ³	25
Figure 39. Metallography image 0.63 cm from top of fuel zone. Fission density $\sim 1.3\text{E}+21$ fissions/cm ³	26

Figure 40. Metallography image 0.63 cm from top of fuel zone. Fission density $\sim 1.3\text{E}+21$ fissions/cm ³	26
Figure 41. Metallography image from plate mid line. Fission density $\sim 2.8\text{E}+21$ fissions/cm ³	26
Figure 42. Metallography image from plate mid line. Fission density $\sim 2.8\text{E}+21$	26
Figure 43. Longitudinal metallography sample from 28 cm from bottom of fuel zone. Fission density $\sim 2.8\text{E}+21$ fissions/cm ³	26
Figure 44. Longitudinal metallography sample from 28 cm from bottom of fuel zone. Fission density $\sim 2.8\text{E}+21$ fissions/cm ³	26
Figure 45. Metallography image 7 cm from bottom of fuel zone. Fission density $\sim 2.0\text{E}+21$ fissions/cm ³	27
Figure 46. High magnification image of ZH4 fuel foil 0.63 cm from top of fuel zone. Fission density $\sim 1.3\text{E}+21$ fissions/cm ³	27
Figure 47. Image of ZH4 fuel foil end at plate mid plane. Fission density $\sim 2.8\text{E}+21$ fissions/cm ³	28
Figure 48. Image of U-Mo/Zr/Al interface at plate mid plane. Fission density $\sim 2.8\text{E}+21$ fissions/cm ³	28
Figure 49. Image of oxide layer formed on plate ZH4.	29
Figure 50. Image of inclusion phase in ZH4 fuel foil 28 cm from bottom of fuel zone.	29
Figure 51. Image of inclusion phase in ZH4 fuel foil.	30
Figure 52. Image of inclusion phase in ZH4 fuel foil.	30
Figure 53. Montage of region with inclusion phase in ZH4 fuel foil.....	30
Figure 54. AFIP-7 plate 7ZH1, front side, showing blistered region of plate.....	33
Figure 55. AFIP-7 plate 7ZH1, back side, showing blistered region of plate.	34
Figure 56. AFIP-7 plate 7ZH3, front side, showing blistered region of plate.....	35
Figure 57. AFIP-7 plate 7ZH3, back side, showing blistered region of plate.	35
Figure 58. AFIP-7 blister threshold results versus average fission density with historical data from previous monolithic blister threshold tests and the 95% upper and lower confidence intervals.	36
Figure 59. AFIP-7 blister threshold results versus plate peak fission density with historical data from previous monolithic blister threshold tests and the 95% upper and lower confidence intervals.	36
Figure 60. Longitudinal gamma scans scaled to experimentally measured chemical burn-up.	38
Figure 61. Fission density plots determined by scaling the gamma scan data.	39
Figure 62. Chemical burn-up scaled gamma scans compared to calculated fission density profiles.....	40
Figure 63. Fuel swelling contour of all AFIP-7 plates.	41
Figure 64. AFIP-7 fuel swelling versus fission density with Kim and Hoffman swelling correlation.	42
Figure 65. AFIP-7 binned swelling versus fission density for each plate with “Kim and Hofman, 2011” swelling correlation.....	43

Figure 66. Least squares fit of binned swelling versus fission density with 95% confidence limits.	44
Figure 67. All AFIP–7 swelling versus fission density with fuel swelling correlation.	45
Figure 68. Monolithic blister threshold temperature data with separate trend models for mini-plates and larger plate geometries.....	46
Figure 69. Pre-irradiation scanning electron image of inclusion phase similar to that observed during post irradiation examination.....	47

TABLES

Table 1. As-built dimensions.	2
Table 2. Fuel foil data.	3
Table 3. ICP-MS results for each sample used to calculate depletion	31
Table 4 AFIP–7 Blister threshold test specimens with pertinent irradiation conditions.....	32

ACRONYMS

AFIP	ATR Full Sized in Center Flux Trap Position
Al	aluminum
ATR	Advanced Test Reactor
BWXT	BWX Technologies
EFPD	effective full power days
EOL	end of life
FD	Fuel Development
HEU	highly enriched uranium
HFEF	Hot Fuel Examination Facility
HPGe	high-purity germanium
ICP-MS	inductively coupled plasma mass spectrometry
INL	Idaho National Laboratory
L2AR's	local to average ratios
LANL	Los Alamos National Laboratory
LEU	low enriched uranium
MCNP	Monte Carlo N-Particle
NQA-1	Nuclear Quality Assurance-1
PGS	precision gamma scanner
PLN	Plan
U-10Mo	Uranium 10 wt% molybdenum alloy
USHPR	United States High Performance Research Reactor
ZR	zirconium

AFIP-7 Post-irradiation Examination Summary Report

1. INTRODUCTION AND EXPERIMENT DESCRIPTION

The U.S. DOE Material, Management and Minimization's United States High Performance Research Reactor (USHPRR) -Fuel Development (FD) pillar is tasked with developing and qualifying a new high density low enriched uranium (LEU) fuel in support of the conversion of high performance research and test reactors from highly enriched uranium (HEU) to LEU.¹ The FD pillar previously conducted a series of mini-plate and prototypic scale plate experiments that led to the selection of a fuel design (referred to as base monolithic fuel) consisting of a uranium-10 wt% molybdenum alloy (U-10Mo) in the form of a monolithic foil, with thin zirconium (Zr) diffusion barrier interlayers, clad in 6061 aluminum (Al) by hot isostatic pressing.²

The AFIP-7 experiment was an applied development irradiation test designed to evaluate the performance of base monolithic U-Mo fuel in geometries that are prototypic of US HPRR fuel plates.³ The experiment contained four formed fuel plates in a curved geometry, as is prototypic of several USHPRR fuel designs that were swaged into a miniature fuel element. Figure 1 shows a cross section of the element. The U-Mo fuel foils were produced via hot and cold rolling, the zirconium interlayer was applied via co-rolling and the cladding was applied using a hot isostatic pressing technique. Details of the fabrication can be found in the fuel fabrication report.⁴ The fuel plates were nominally 101 cm \times 6.2 cm \times 1.27 mm with a nominal fuel zone of 98 cm \times 5.5 cm \times 0.33 mm, as shown in Figure 2. Each U-Mo fuel foil had a nominally 25 μ m zirconium diffusion barrier applied via co-rolling to both faces. A schematic cross sectional view of the fuel plate with the diffusion barrier can be seen in Figure 3.

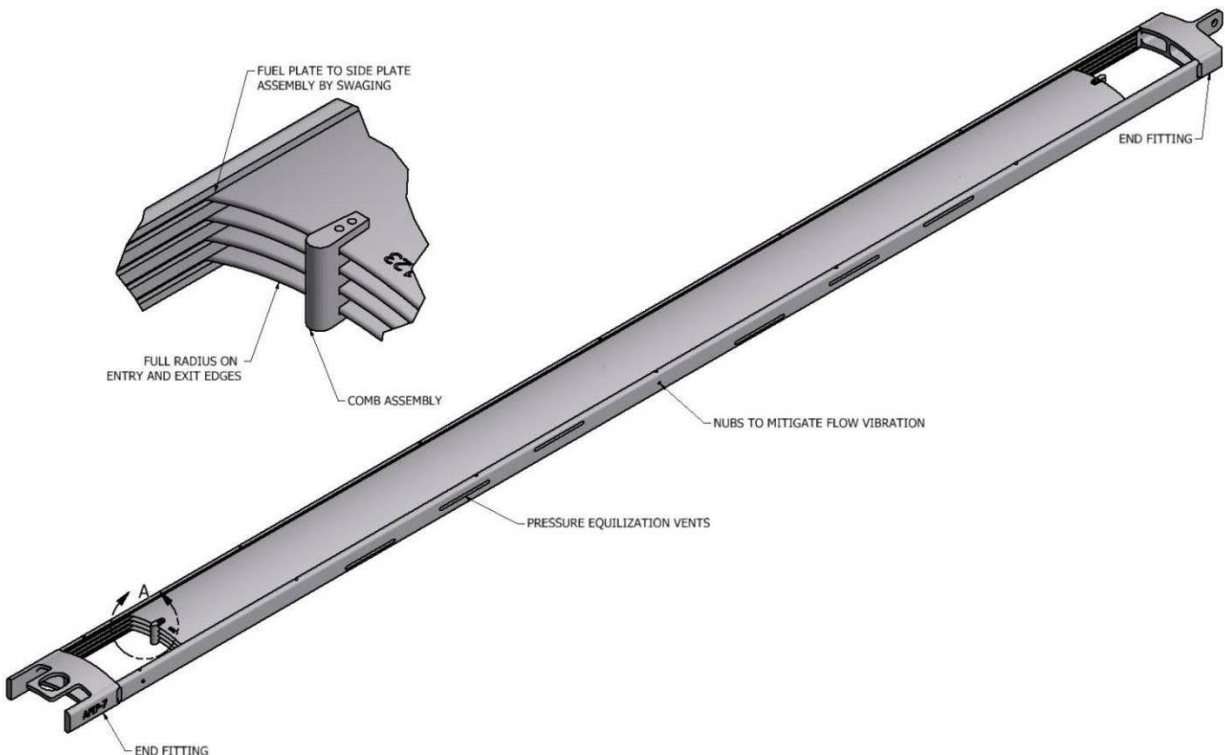


Figure 1. Isometric view of the AFIP-7 element.⁶

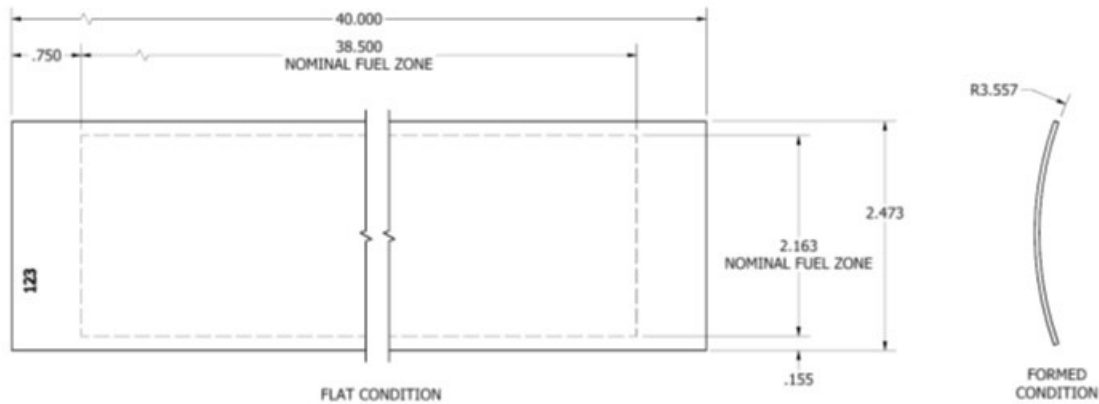


Figure 2. AFIP-7 Plate Drawing.

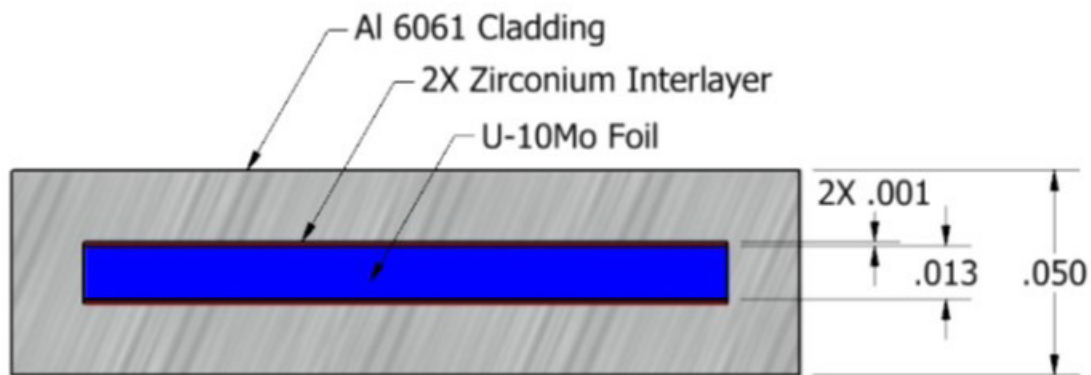


Figure 3. AFIP-7 Nominal Fuel Plate Cross Section.

Final as-built dimensions of the four fuel plates and fuel foils can be found in Table 1. Mass data of the fuel plates and fuel foils can be found in Table 2. The fuel foil used for plate ZH1 was rolled at the Y-12 National Security complex and the fuel foils for the remaining plates were rolled at Los Alamos National Laboratory (LANL). All plate fabrication and element assembly including hot isostatic pressing was performed at BWX Technologies incorporated (BWXT).

Table 1. As-built dimensions.

Plate	Foil Length (mm)	Avg Foil Width (mm)	Avg Foil Thickness (mm)	Plate Length (mm)	Plate Width (mm)	Plate Thickness (mm)	Curvature Radius [mm]
ZH-1	990.6	54.02	0.381	1016.25	62.81	1.32	90.35
ZH-2	990.6	55.02	0.383	1015.95	62.87	1.32	90.35
ZH-3	983.49	55.02	0.381	1016.14	62.85	1.31	90.35
ZH-4	990.6	54.94	0.384	1016.25	62.78	1.32	90.35

Table 2. Fuel foil data.

Plate ID	Foil Fabrication Location	Fuel Plate Mass (g)	Fuel Phase Constituent Masses				Interlayer Phase Mass (estimated)	Cladding Mass (estimated)
			U-Mo Fuel Phase (g)	Total U (g)	U-235 (g)	Mo (g)	Zr (g)	Al-6061 (g)
7ZH-1	Y-12	479.21	283.07	251.81	49.26	31.26	19.23	176.91
7ZH-2	LANL	500.26	314.03	283.71	56.13	30.32	14.11	172.12
7ZH-3	LANL	492.00	304.57	271.48	53.97	33.09	15.66	171.77
7ZH-4	LANL	503.71	313.95	283.64	56.11	30.31	14.10	175.66

Flow testing of the AFIP-7 element was performed to verify design calculations and provide feedback into irradiation condition calculations. Analysis of the results from this testing are currently underway and will be outlined in a flow testing report to be published.⁵

2. IRRADIATION HISTORY

The AFIP-7 experiment was irradiated in the center flux trap of the advanced test reactor. The experiment was irradiated for two cycles, 149B (54.6 EFPD's) and 150B (42 EFPD's) for a total of 96.6 effective full power days (EFPD's). Configuration of the four plates within the element can be seen in Figure 4. Monte Carlo N-Particle (MCNP) code, ORIGEN2.2 and MCWO were utilized for neutronic calculations.⁷

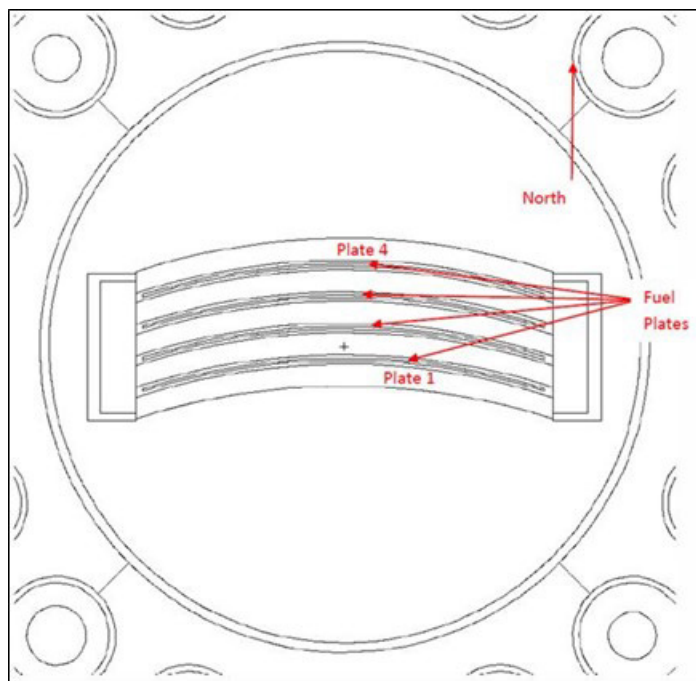


Figure 4. MCNP model X-Y view of the AFIP-7 test assembly.

Calculations were performed at four time steps during each irradiation cycle including beginning-of-cycle, two mid-cycle points, and end of cycle. The lobe power history for each cycle is shown in Figure 5. It can be seen that at the beginning of each cycle there is a spike in the power in the center flux trap position. This resulted in spikes in the power and heat flux for the AFIP-7 plates during reactor startup. The local surface heat flux for each plate at each time step is shown in Figure 6, which clearly shows the higher beginning of life (BOL) heat flux during the first time step.

End of life (EOL) fission densities were calculated for 78 equal sized transverse slices down the length of the plates in order to provide a longitudinal profile. Calculation results indicate a peak fission density of approximately $2.9\text{E}+21$ fissions/cm³ for plate ZH4 at approximately the midline of the plate. Plates ZH1, ZH2 and ZH3 are all similar with peaks approximately $2.6\text{E}+21$ fissions/cm³. Longitudinally calculated fission densities for each plate are shown in Figure 7.

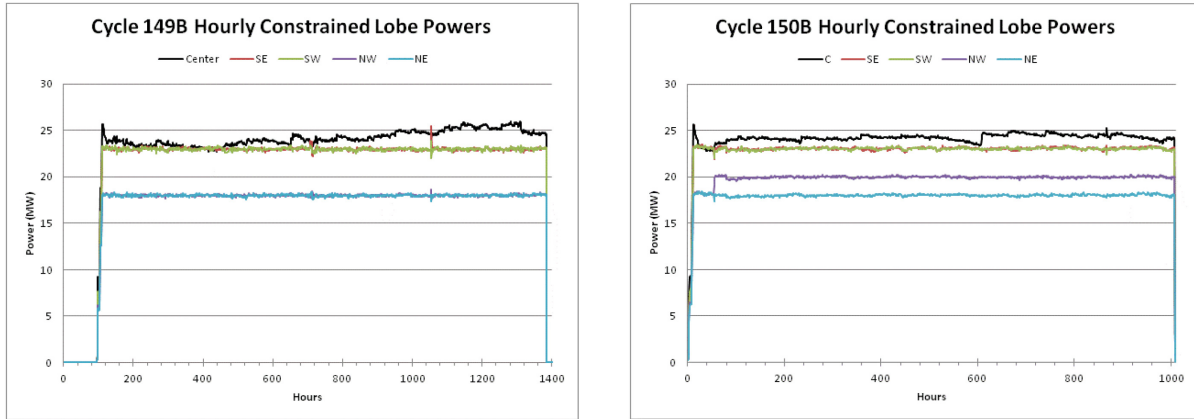


Figure 5. Hourly constrained lobe power history for cycles 149B (left) and 150B (right).

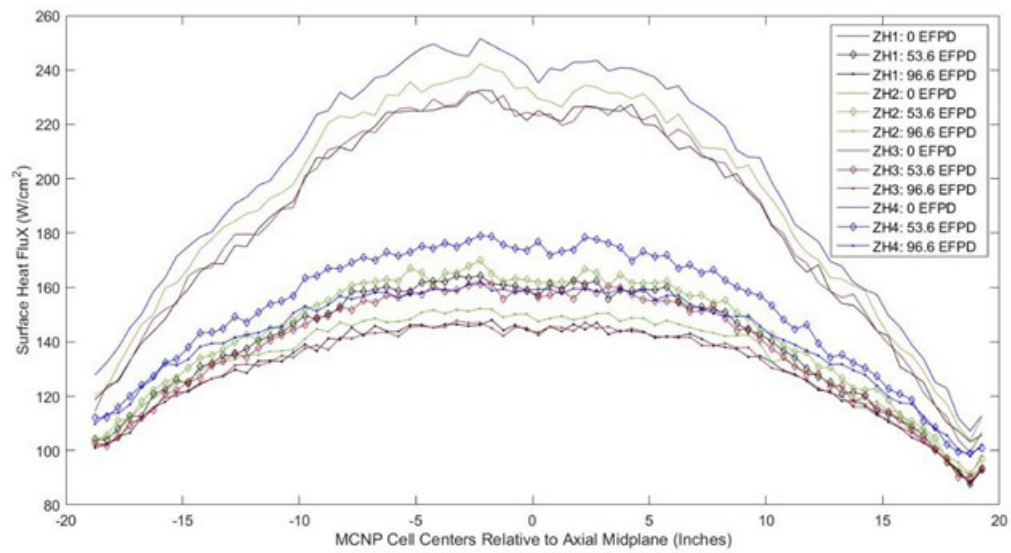


Figure 6. Fuel plate surface heat flux during irradiation.

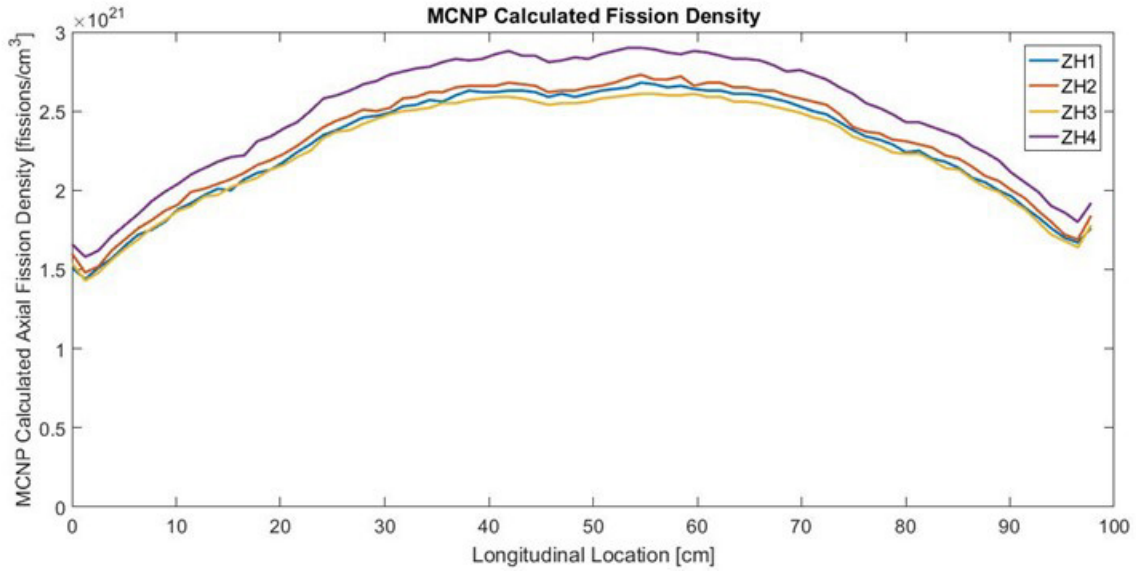


Figure 7. MCNP calculated longitudinal end of life fission densities.

In order to calculate transverse gradients over the plates, each of the 78 longitudinal nodes was subdivided into 20 equal-sized nodes and local to average ratios (L2AR's) were calculated for each slice. These L2AR's provide the BOL power and fission density gradient values across the plate width at each node and can be used to create a two dimensional profile over the plate. These two dimensional fission density profiles can be seen in Figure 8. The fission density gradients for all four plates show the highest fission density at the edges of the plates at the longitudinal mid-plane.

Prior to irradiation and subsequently after each irradiation cycle, channel gap measurements were taken in the ATR canal. This was performed using an ultrasonic probe lowered into each channel gap on specific line traces. The results from the channel gap measurements indicate that the channel gaps were stable during the irradiation.⁸

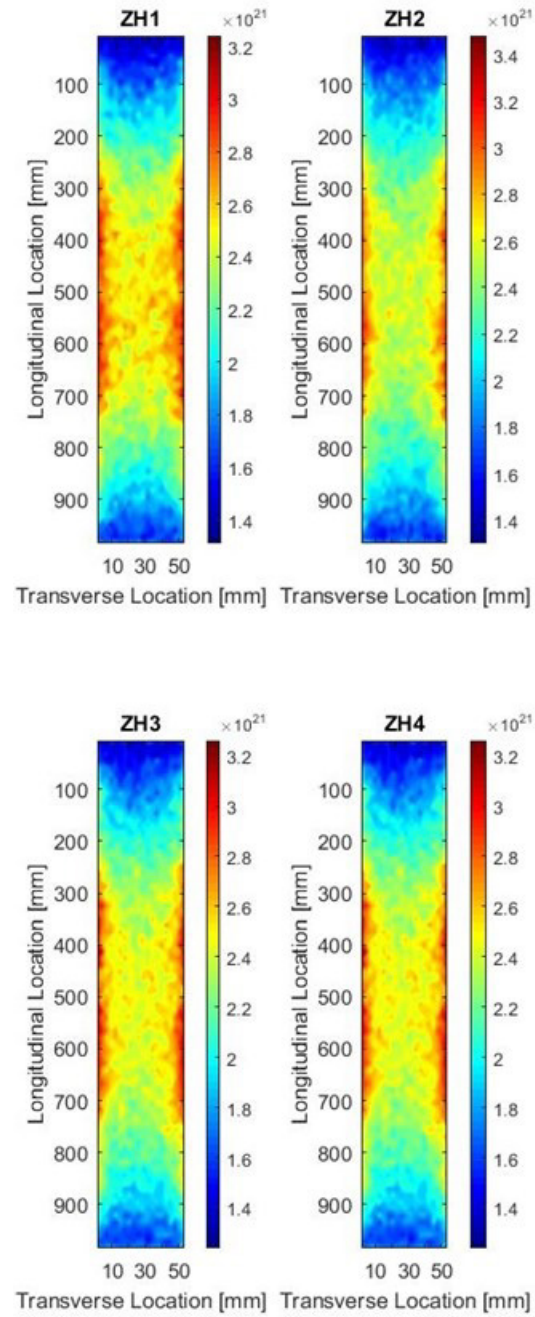


Figure 8. MCNP calculated fission density distributions for each fuel plate.

3. NON DESTRUCTIVE POST IRRADIATION EXAMINATION RESULTS

Following irradiation and cooling, the experiment was transferred to the INL's Hot Fuel Examination Facility (HFEF) for post-irradiation examination, where it was stored in the shipping cask insert for approximately four years prior to the start of post irradiation examinations.

Post irradiation examinations are performed to demonstrate that the fuel meets irradiation performance requirements for mechanical integrity, geometric stability, and stable and predictable behavior.

The post irradiation exams performed are described along with their intent. Nondestructive examinations are performed first and are used to guide destructive examinations to follow. All data acquisition is done using NQA-1, Part 1 requirements and are outlined in approved test plans. These test plans call out training and calibration requirements, testing requirements, and data acceptance and reporting requirements. Test plans were written to direct neutron radiography (PLN-4466 and 5011), gamma scanning (PLN-4536), profilometry (PLN-4509), blister threshold testing (PLN-5213), sectioning (PLN-4612), and microscopy (PLN-4643).

Visual examination of both the fuel element and the fuel plates is performed to identify any changes that may have occurred during irradiation or shipping. This is performed using through-window photography. Neutron radiography is performed in order to non-destructively interrogate the fuel within the cladding and is used to identify any fuel cracking or relocation. Gamma scanning is performed to investigate the distribution of fission products both longitudinally and transversely within the fuel plate. The gamma scans provide relative measures of the fission density distribution within the fuel. Profilometry and eddy current measurements are performed to investigate plate dimensional changes, specifically in the thickness direction (fuel swelling) and oxide layer growth on the surface of the plate, respectively.

Typical destructive examinations include sectioning for optical metallography and chemical analysis. Additionally, two of the intact fuel plates were subjected to blister threshold testing. Optical metallography identifies microstructural changes in the fuel and investigates the interfaces between the fuel, diffusion barrier and cladding. Chemical analysis is used to validate the MCNP calculated burn-up values. Blister threshold testing is performed to identify the temperature at which blister formation occurs, which is important for establishing fuel operating temperature limits used in reactor safety analysis.

The nomenclature for orientation of the plates during post irradiation examination refers to the "top" of the plate being the end with the ID stamp. "Left" and "right" are the sides of the plate when looking at the face of the plate with the ID stamp.

3.1 Disassembly and Fixturing

In order to remove the fuel plates from the element, the frame of the assembly had to be machined away to release the swage joint that held the fuel plates. This was done by building a frame to hold the assembly horizontal with the end block material exposed, as shown in Figure 9. A precision mill equipped with an end mill was first used to mechanically machine the comb separating the plates at the top of the element, as shown in Figure 10, and then remove the end block material to free the plates, Figure 11.

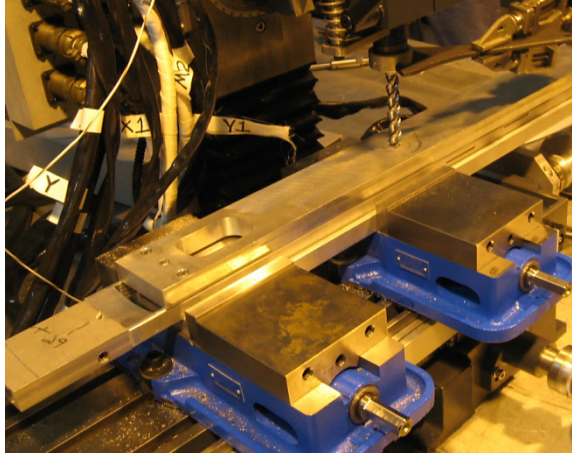


Figure 9. AFIP-7 dummy element in milling fixture.

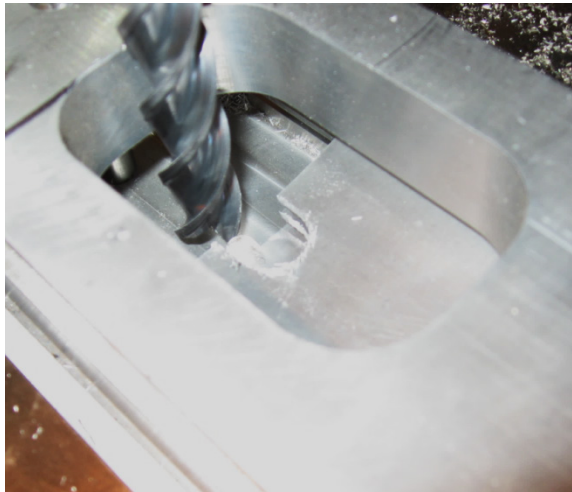


Figure 10. Machining the spacer comb from the fuel element.

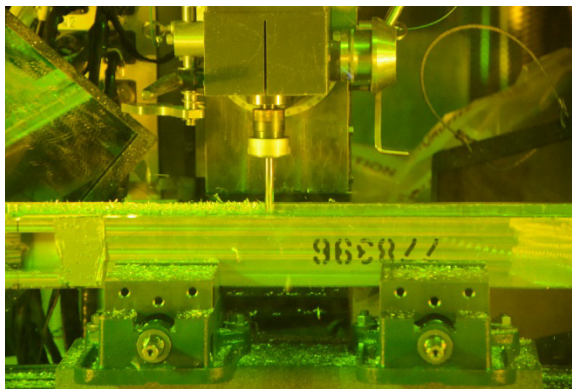


Figure 11. Machining end block material from the AFIP-7 element.

After the plates were removed from the element they were loaded into a picture frame-style strong-back. This prevented the plates from being damaged due to handling and allowed the plates to be moved throughout the hot cell for the subsequent examinations.

3.2 Visual Examination

After the plates were loaded into the strong-backs, visual examination of each plate was performed using through-window photography. This was done to identify any anomalies or damage that may have occurred due to shipping or handling of the element. Each strong-back was equipped with a ruler to assist with examination. Both the front and back of each plate were photographed at high and low magnification.

Montages of the low magnification images taken of the front of each plate are shown in Figure 12. Lighting differences on the plate surface create apparent non-uniformities when the images are stitched together, especially on the lower magnification images. Higher magnification images have been examined and no damage or defects on the plate surfaces was found. An example of a higher magnification image is shown in Figure 13.

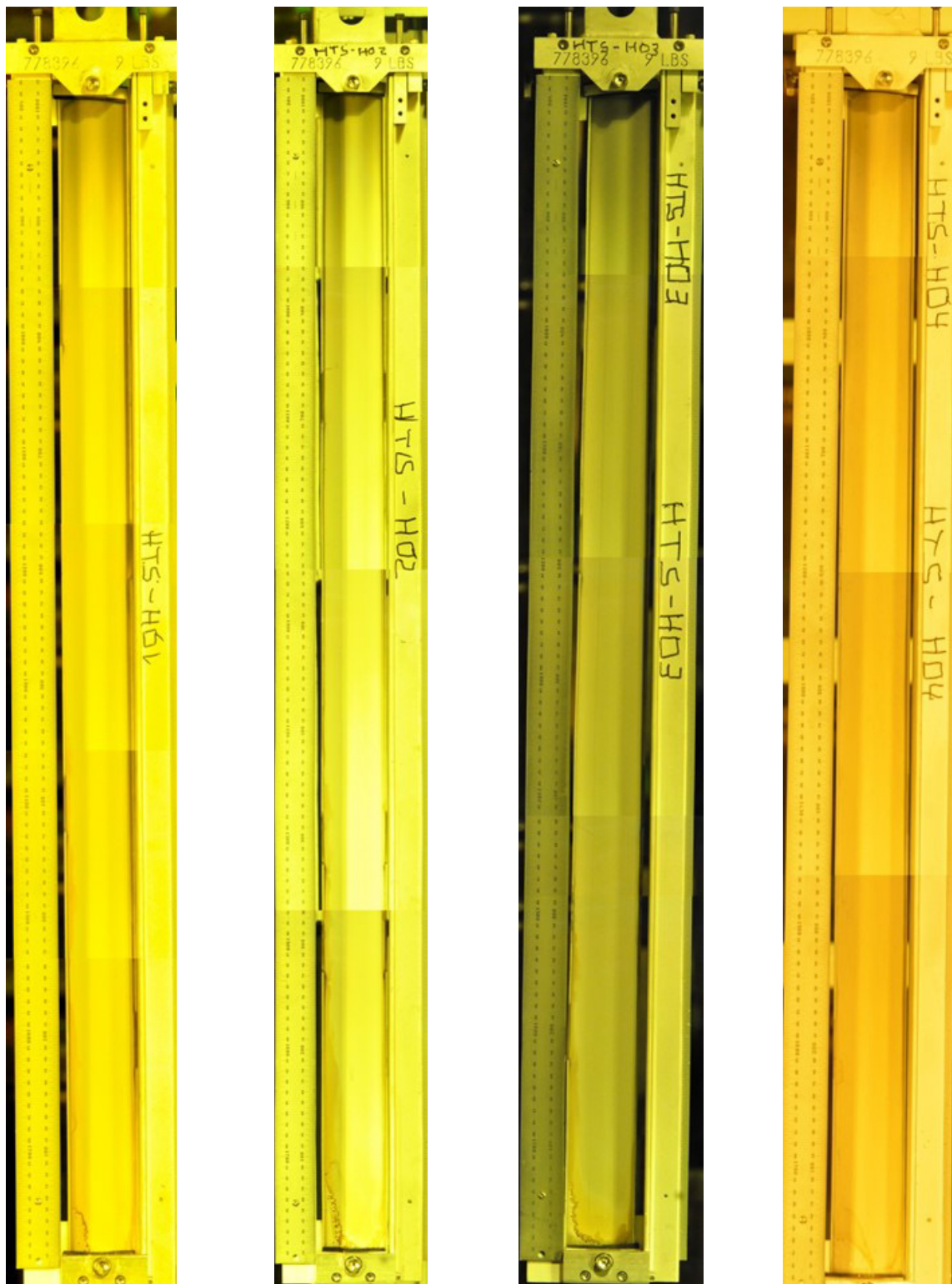


Figure 12. Visual examination montage of plate faces ZH1 through ZH4 (left to right).

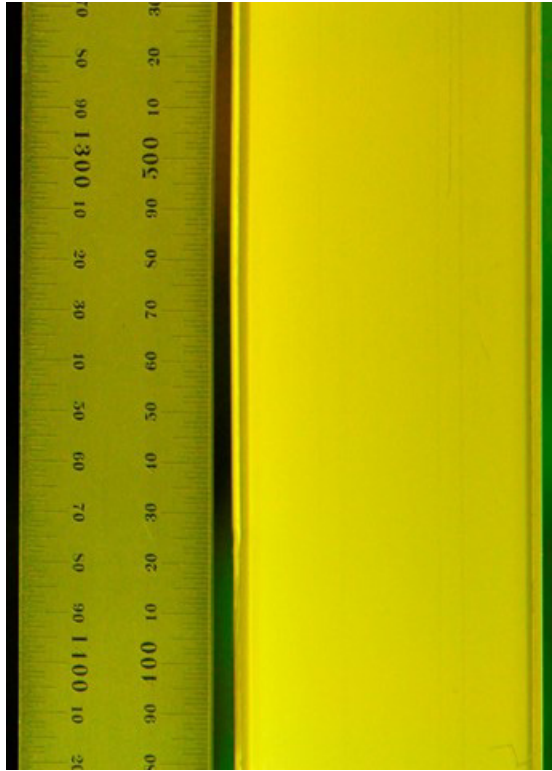


Figure 13. Visual examination image from ZH3.

During visual examination of the plates a foreign substance was observed at the bottom of the fuel plates. The substance appeared to be a hardened, viscous material and was on the front and back surface of each of the four plates. The substance appeared to have wicked from the bottom of the plates upward and could be seen on the bottom 1-2 inches of each of the plates. At this time, the composition of the substance is unknown but is hypothesized to be oil from a leaking hot cell window that may have come in contact with the plates during the long storage period in the hot cell. Figure 14 shows the substance at the bottom of plate ZH4 which also shows shavings from the element disassembly embedded in it. Initial visual examinations performed on the element upon receipt in 2011 did not indicate the presence of the substance on the plates, therefore supporting the assumption that this surface contamination occurred during the long-term storage of the element in the hot cell. Initial attempts to sample the material for compositional analysis were unsuccessful.

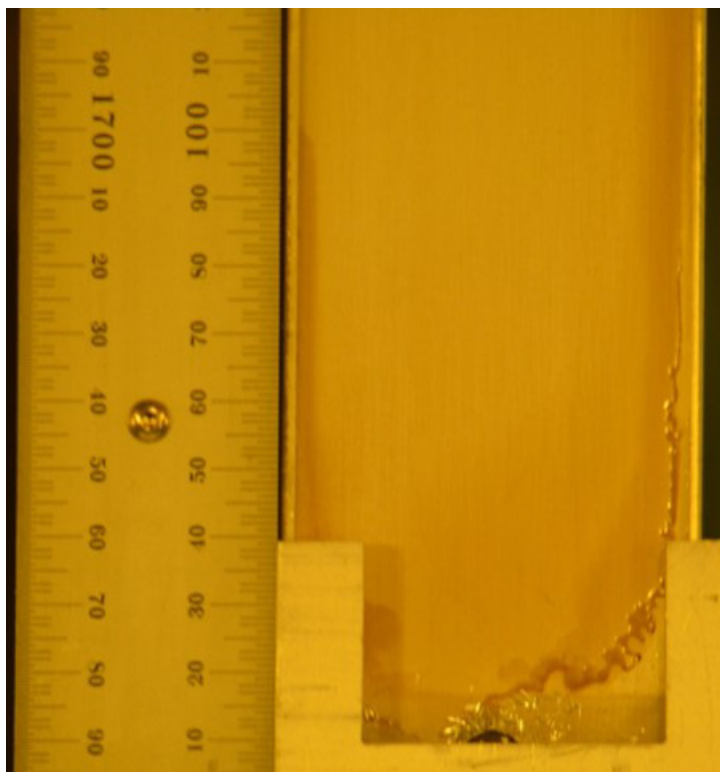


Figure 14. Visual examination image from the bottom of ZH4.

3.3 Neutron Radiography

Neutron radiography was performed on all four AFIP-7 fuel plates to identify any fuel cracking or relocation that may have occurred within the plate during irradiation. The plates were radiographed in the strong-backs and the rulers, doped with gadolinium, can be seen in the images for reference. Neutron radiography is performed with two different neutron energies, thermal and epithermal, in order to provide varying contrast.

No fuel cracking was observed in any of the images and none of the radiographs showed anything remarkable, which indicates the fuel likely performed acceptably. Examples of these results can be seen in Figure 15 and Figure 16 for the thermal and epithermal images, respectively, for plate ZH1.

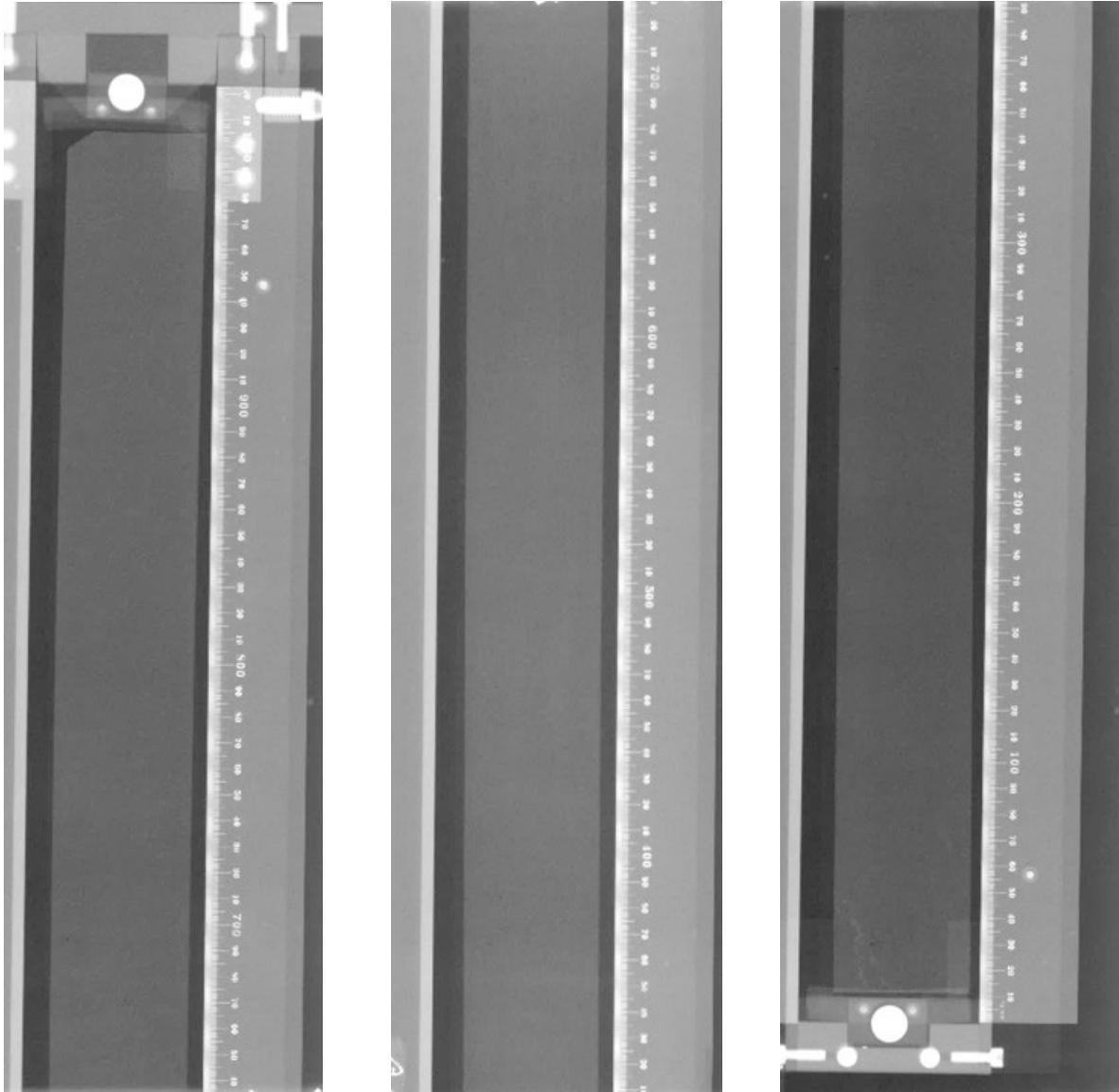


Figure 15. Thermal Radiographs of AFIP-7 ZH1 from top to bottom.

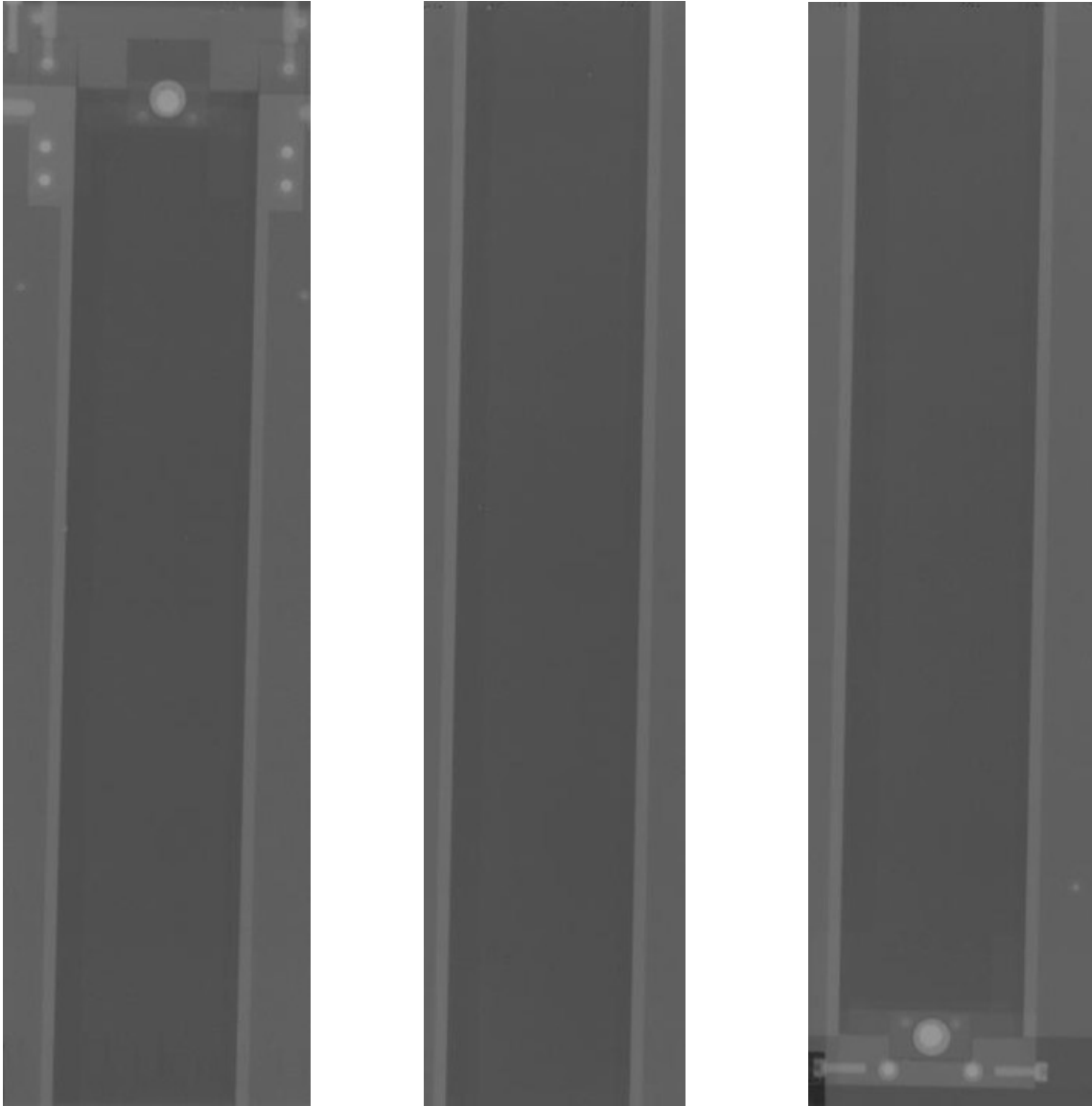


Figure 16. Epithermal Radiographs of AFIP-7 ZH1 from top to bottom.

3.4 Gamma Scanning

Gamma scanning was performed using the HFEF precision gamma scanner (PGS). The PGS system consists of a collimator that penetrates the HFEF hot cell wall, a high-purity germanium (HPGe) gamma-spectrometry system, and an in-cell elevator used to position samples for examination. The in-cell side of the collimator consists of tungsten alloy blocks that can be adjusted to create a slit height varying from 2.54–0.0254 mm. The width of the collimator opening is fixed at 22.22 mm, creating a rectangular viewing area for the PGS system. The slit is fixed horizontal for longitudinal scans and rotated to vertical for transverse scans. Gamma rays entering the collimator travel through the hot cell wall, through a second tungsten-alloy beam scraper, and then to the HPGe detector.

Gamma scanning is performed to measure the relative burn-up profiles over the plates, both longitudinally and transversely, as well as to look for any unexpected fission product migration within the fuel plates. The main isotopes of interest included Ce-144, Cs-137, and Pr-144. Cs-137 was used for analysis due to its long half-life and isotopic abundance.

Scans were performed longitudinally down the length of the plates with 2.54 mm spacing. Figure 17 shows the relative axial scans from top (left) to bottom (right) of all four plates. Analysis of the profiles shows that plate ZH4 had the highest relative burn-up, which agrees with the MCNP calculations.

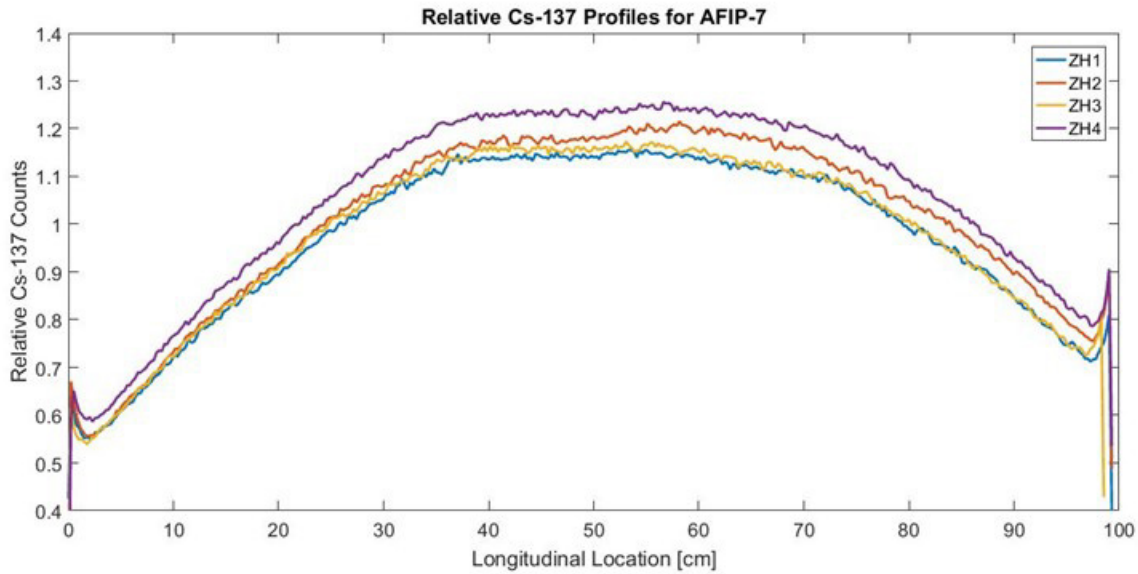


Figure 17. Longitudinal gamma scan profiles.

Transverse scans across the plate widths were taken at five locations on each plate (approximately 32, 260, 490, 717, and 946 mm from the top of the fuel zone) to examine edge peaking and any transverse fission density gradient. Transverse scans were performed with 0.254 mm spacing. The five scans for each plate are shown in Figure 18. All scans showed some degree of edge peaking and increased relative counts in the higher burn-up regions, as expected. Plates ZH2, ZH3 and ZH4 all showed burn-ups shifted slightly higher toward the left side of the plate, although the distributions were smooth. Plate ZH1 showed a relatively level burn-up profile across the plate width. There was no unanticipated migration of any isotopes observed in either the transverse or longitudinal gamma scans.

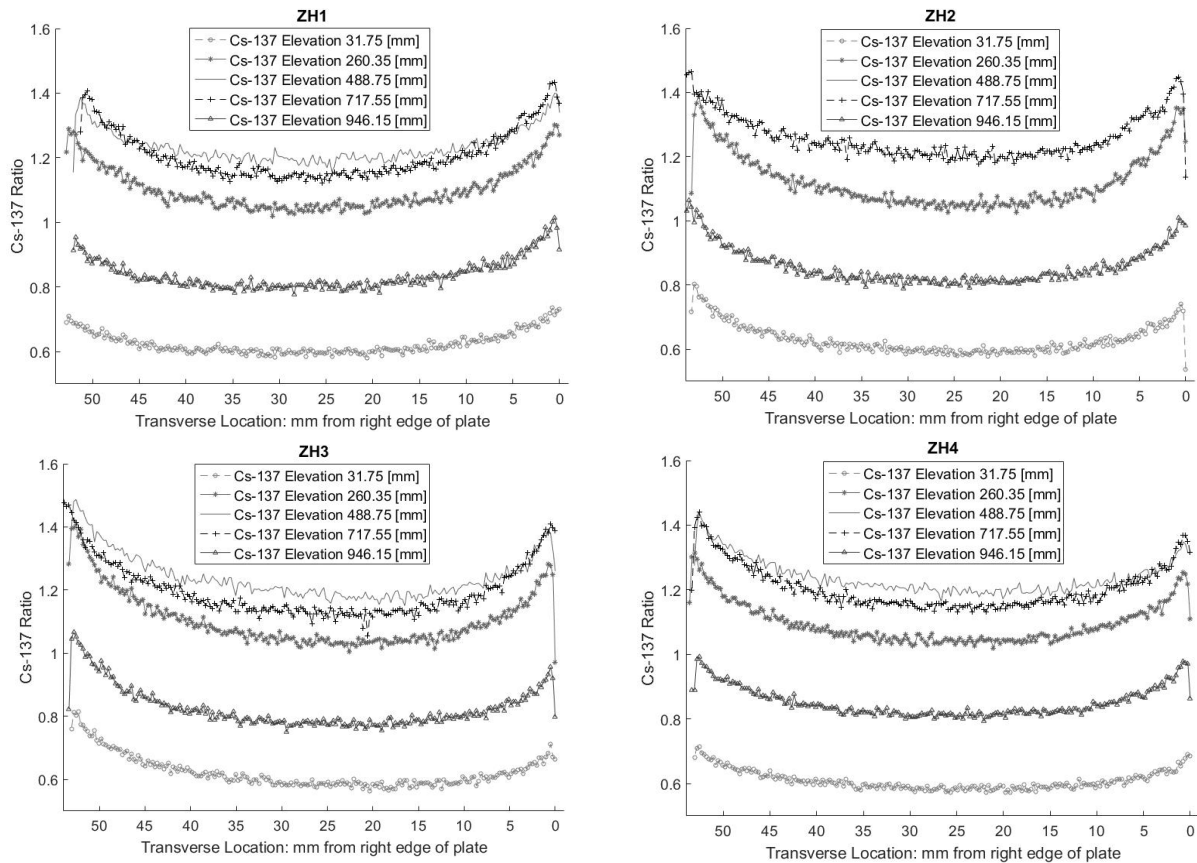


Figure 18. CS-137 transverse gamma scan profile for all plates.

3.5 Profilometry and Eddy Current

In order to quantify plate dimensional changes and local fuel swelling, each of the four plates was subject to profilometry and eddy current inspection. This was performed using the BONA4INL measurement bench. This bench was designed specifically to accommodate and measure AFIP-7 curved fuel plates. The plates are clamped at both ends and a measurement head is driven longitudinally down the length of the plates. The fuel plates are rotated between line scans to incrementally move transversely over the plates. The measurement head is equipped with two opposing, customized Sony Magnescale contact probes, which provide plate thickness values. Ceramic thickness standards of 1, 1.5 and 2 mm are used to calibrate the probes prior to measurements.

Simultaneously, eddy current probes in contact with the plate surface measure oxide thickness. Certified Mylar foils are used for calibration of the eddy current probes prior to measurements. The thickness of the aluminum oxide corrosion layer on the fuel plate surface was measured to support analysis of the fuel plate thermal conditions. Because the thermal conductivity of the corrosion layer is low, thin layers can have a meaningful impact on the fuel meat temperature during irradiation. The measurement bench prior to installation can be seen in Figure 19 loaded with a dummy AFIP-7 fuel plate for qualification.

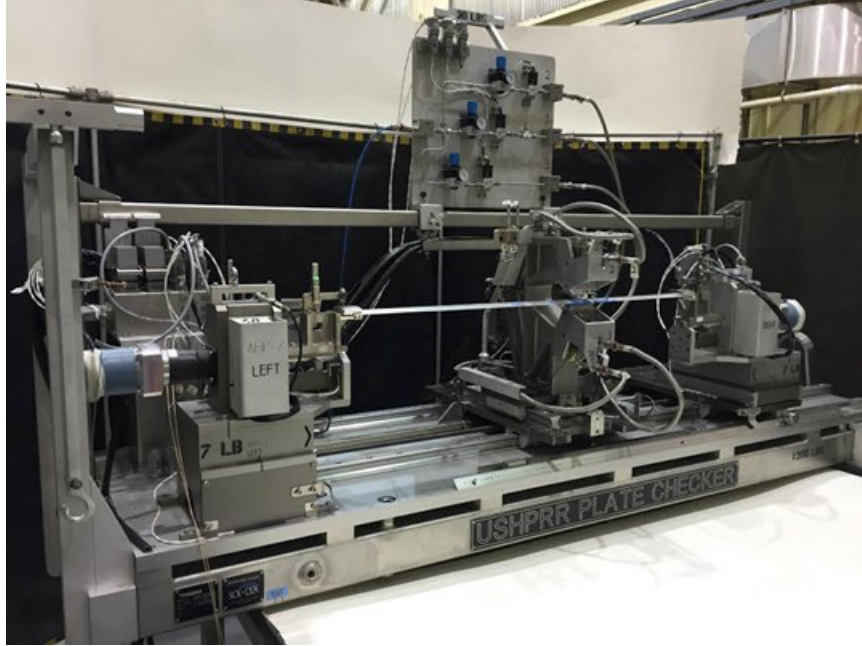


Figure 19. BONA4INL USHPRR Plate Checker prior to installation into HFEF.

The measurement bench can collect data on various measurement grids. For the AFIP-7 campaign, the measurement grid was set at 2 measurements per millimeter in the longitudinal direction and the plates were rotated 2 degrees (approximately 3mm) between line scans. This resulted in approximately 36,000 thickness points over the plate and 36,000 oxide measurements on each side of the plate.

Due to the foreign substance found at the bottom of the plates (section 3.2), this area was intentionally avoided during profilometry and eddy-current testing to avoid damaging the measurement probes or influencing the results. The coordinates of the measurements are aligned such that (0, 0) is set to the top left corner of the fuel zone for each plate. Figure 20 shows the thickness profiles for each of the four plates.

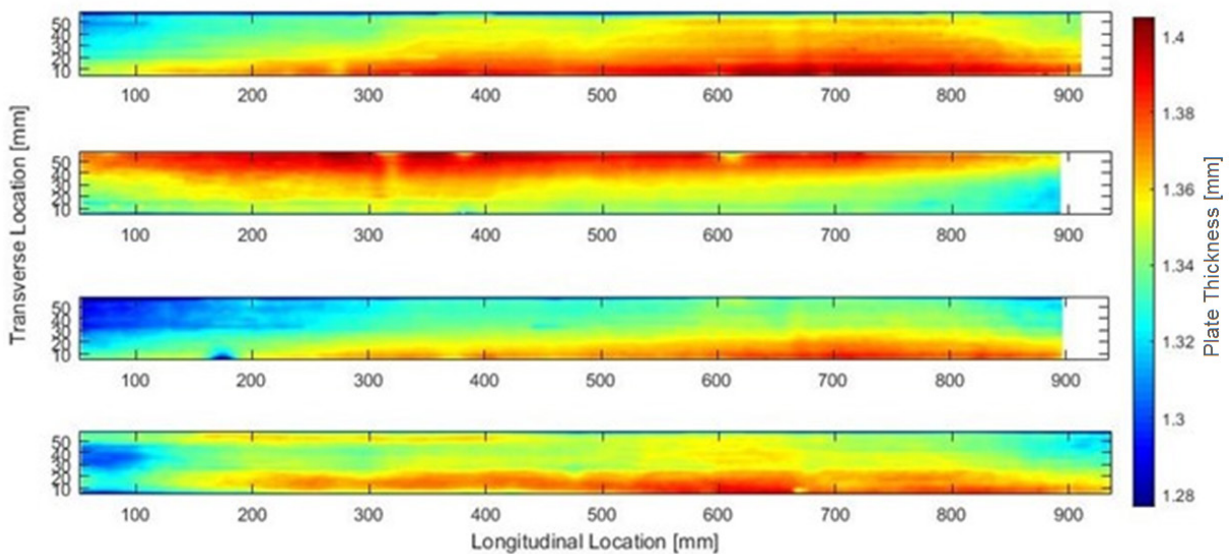


Figure 20. Thickness profiles for ZH1 (top) through ZH4 (bottom).

The longitudinal profiles appear as expected with peak thickness values occurring near peak burn-up areas in the center of the plate. Transverse profiles for ZH1, ZH3, and ZH4 show peak thickness values on the left edge of the plates. Plate ZH2 has a peak thickness on right edge of the plate. Examination of the as built thickness data shows a slight bias in pre-irradiation thicknesses of the plates. Plate ZH2 appeared slightly thicker on the right side of the plate resulting in slightly thicker post irradiation thickness while plates ZH1, ZH3 and ZH4 appeared to be slightly thicker on the left prior to irradiation.

Oxide measurement results are shown in Figure 21 through Figure 24 as line scans down both the front and back of each plate. Measurements at the edges and ends of the fuel zone become erratic due to the nature of eddy current. ASTM standard E376-11 indicates that measurements taken within 3 and up to 13 mm of a discontinuity, such as the edge region of the fuel foil, can be effected and considered invalid.⁹ Some of those variations can be seen in select line scans where values increase significantly more than average. Oxide thickness values for all four plates were seen to be thin and uniform with values peaking at 10-15 microns in thickness with most of the thicknesses falling between 0 and 10 microns.

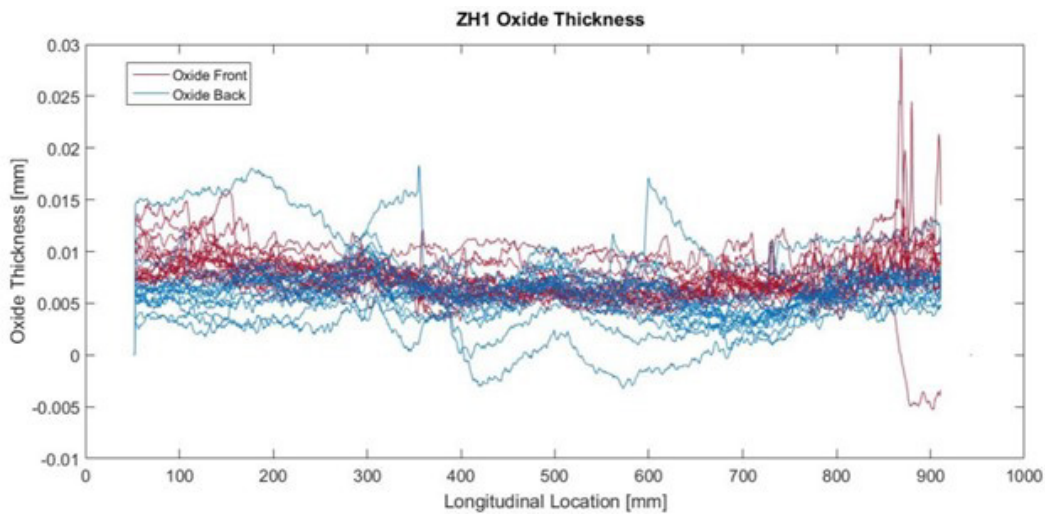


Figure 21. Eddy current results from ZH1.

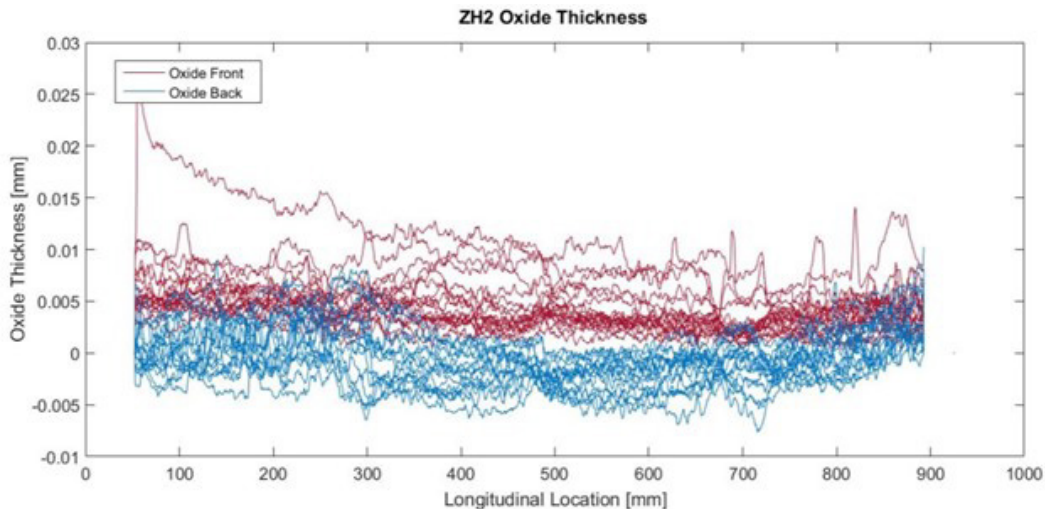


Figure 22. Eddy current results from ZH2.

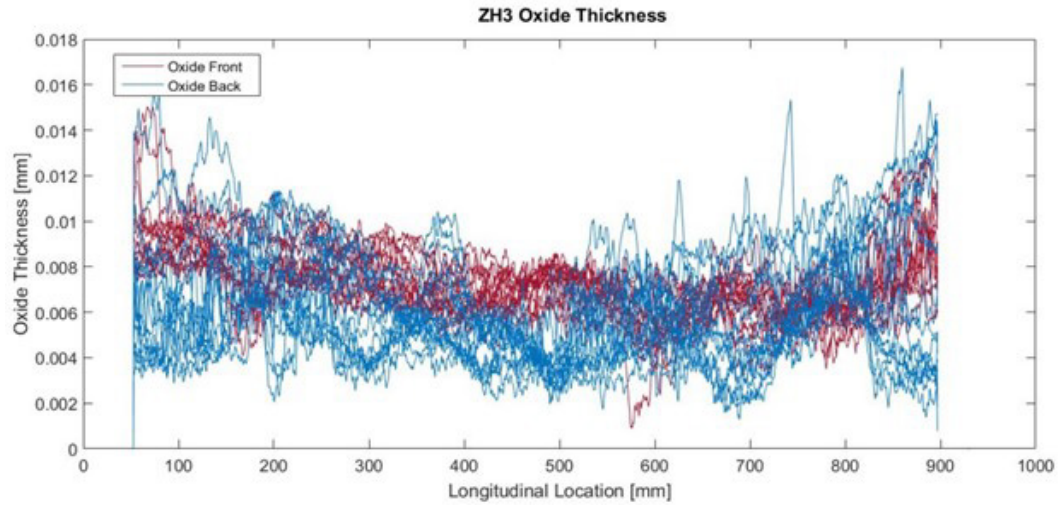


Figure 23. Eddy current results from ZH3.

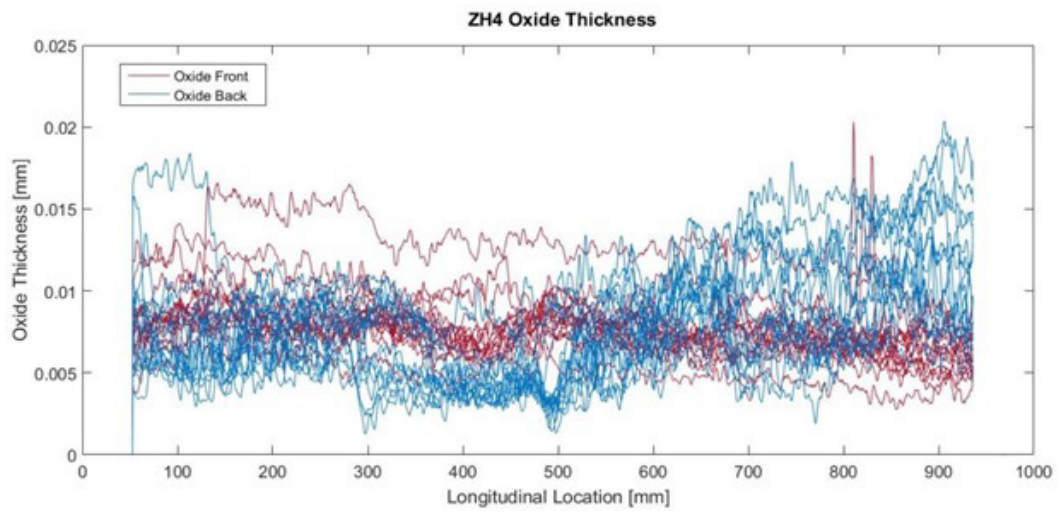


Figure 24. Eddy current results from ZH4.

4. DESTRUCTIVE POST IRRADIATION EXAMINATION RESULTS

Baseline destructive examinations included sectioning two plates for optical metallography and chemical analysis as well as blister threshold testing on two whole plates.

Plates ZH2 and ZH4 were selected for sectioning. This provided an inner and an outer plate from the element. The sectioning diagrams for the two plates are shown in Figure 25. Gold colored sections were collected for optical microscopy, pink samples identify chemical burn-up samples, and blue samples were reserved for future bend testing of the fuel. Bend testing results will be reported later in a separate report.

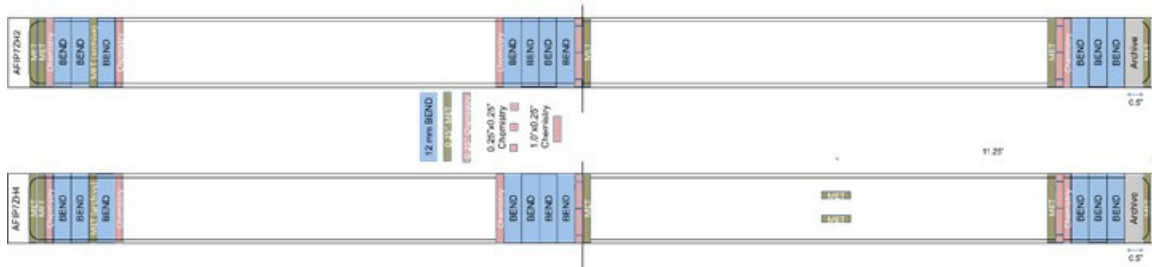


Figure 25. AFIP-7 Sectioning Diagram.

4.1 Metallography

Preparation of optical metallography samples started with cutting 6.3 mm wide cross sections from the identified location on the plate. Each cross section was then sub-sized into 3 pieces approximately 21 mm in length in order to fit into the metallographic mounts. This results in 3 met mount samples being needed to create an entire cross sectional image of the plate.

Each met mount is examined and photographed at 50x magnification in order to capture images for creating a montage of the entire sample cross section. The stitched montage images of the samples are shown below in section 4.1.2.1 and section 4.1.1.1. Montage images are used to identify macroscopic fuel behavior such as non-uniform swelling, fuel cracking, or areas where irradiation enhanced creep has resulted in fuel relocation. Each sample is also subject to higher magnification inspection in order to identify any microstructural changes, interaction layer growth, fission gas morphology, or other pertinent observations.

Cracking was observed in several of the metallography samples originating from the cut interface. No cracking was observed in neutron radiography and there were several examples where two adjacent samples exist with only one of them exhibiting cracking; therefore it is assumed that the cracking occurred during clamping and cutting, as a result of sample curvature not exactly matching the fixture curvature.

4.1.1 Plate ZH2

4.1.1.1 Montages

Low magnification optical metallography montages from plate ZH2 are provided below. This includes the cross sectional samples prepared at the top of the plate, mid plane of the plate and bottom of the plate. Each montage shows one third of an entire cross section from the plate.



Figure 26. Metallography image from top edge of fuel zone. Fission density $\sim 1.5\text{E}+21$ fissions/cm³.

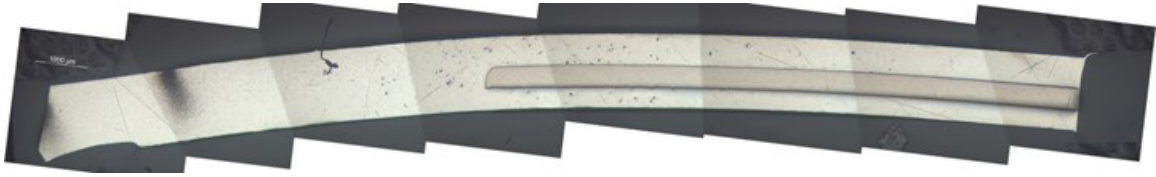


Figure 27. Metallography image from top edge of fuel zone. Fission density $\sim 1.5\text{E}+21$ fissions/cm³.



Figure 28. Metallography image from fuel centerline. Fission density $\sim 2.7\text{E}+21$ fissions/cm³.

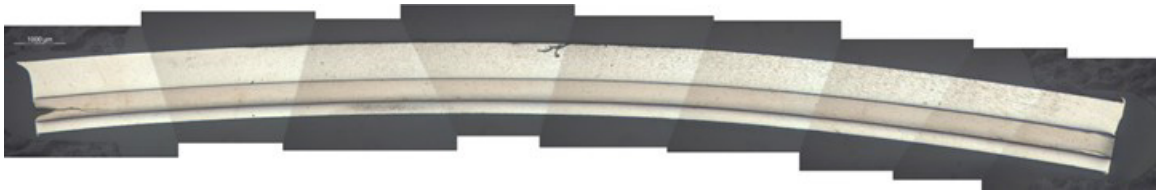


Figure 29. Metallography image from fuel centerline. Fission density $\sim 2.7\text{E}+21$ fissions/cm³.

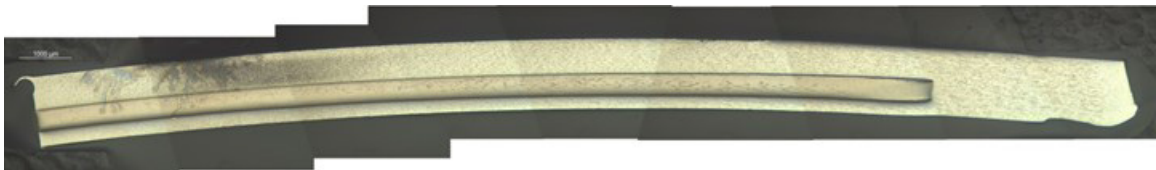


Figure 30. Metallography image 7 cm from bottom of fuel zone. Fission density $\sim 2.0\text{E}+21$ fissions/cm³.

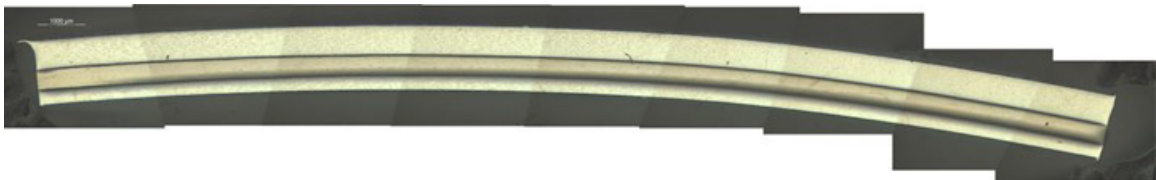


Figure 31. Metallography image 7 cm from bottom of fuel zone. Fission density $\sim 2.0\text{E}+21$ fissions/cm³.

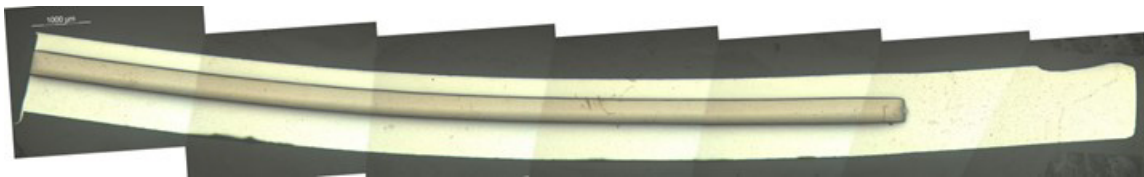


Figure 32. Metallography image 7 cm from bottom of fuel zone. Fission density $\sim 2.0\text{E}+21$ fissions/cm³.

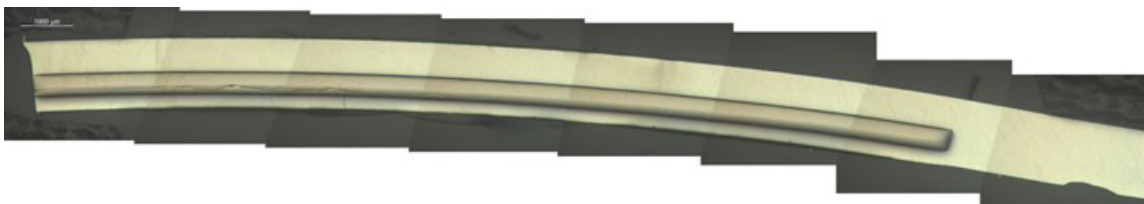


Figure 33. Cross section from bottom edge of fuel zone. Fission density $\sim 2.0\text{E}+21$ fissions/cm³.

4.1.1.2 High Magnification Images

Select, representative high magnification images of plate ZH2 are provided below. Images include regions from the uncovered edge of the fuel foil, U-Mo/Zr/Al interface regions, plate surface images and regions of particular interest within the U-Mo fuel. Dark carbide precipitates can be seen dispersed throughout the fuel and are not unusual for U-Mo fuel. They are small (up to $\sim 5\ \mu\text{m}$) and have not affected fuel performance. Some regions with thinner than nominal ($25\ \mu\text{m}$) zirconium diffusion layer were observed but performance did not appear to be affected in any way, Figure 38.

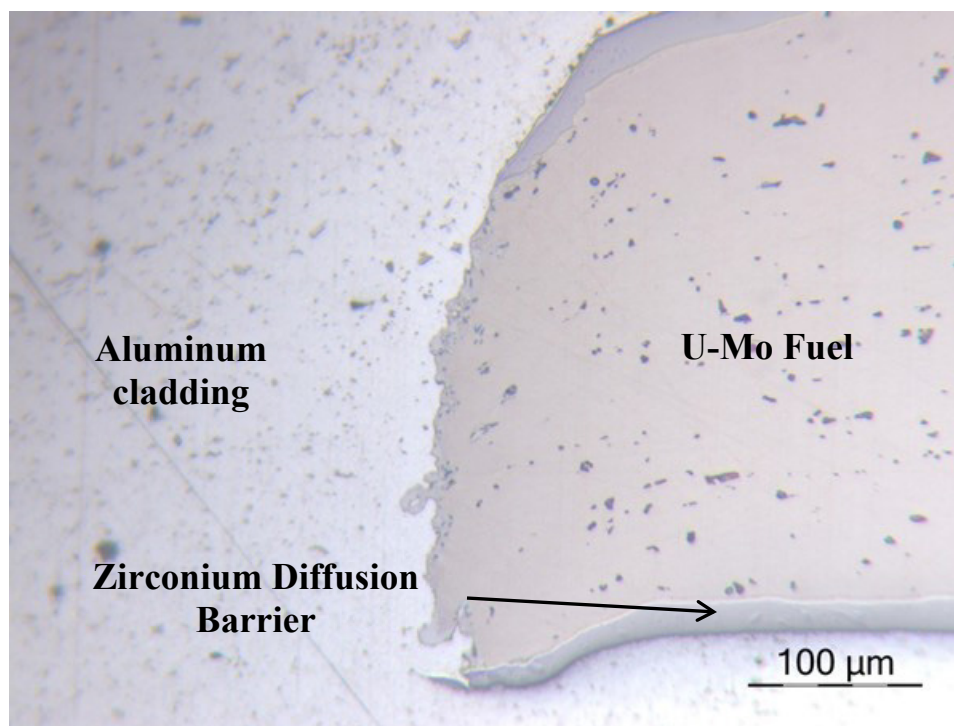


Figure 34. High magnification of ZH2 foil edge at top of fuel zone. Fission density $\sim 1.5\text{E}+21$ fissions/cm³.

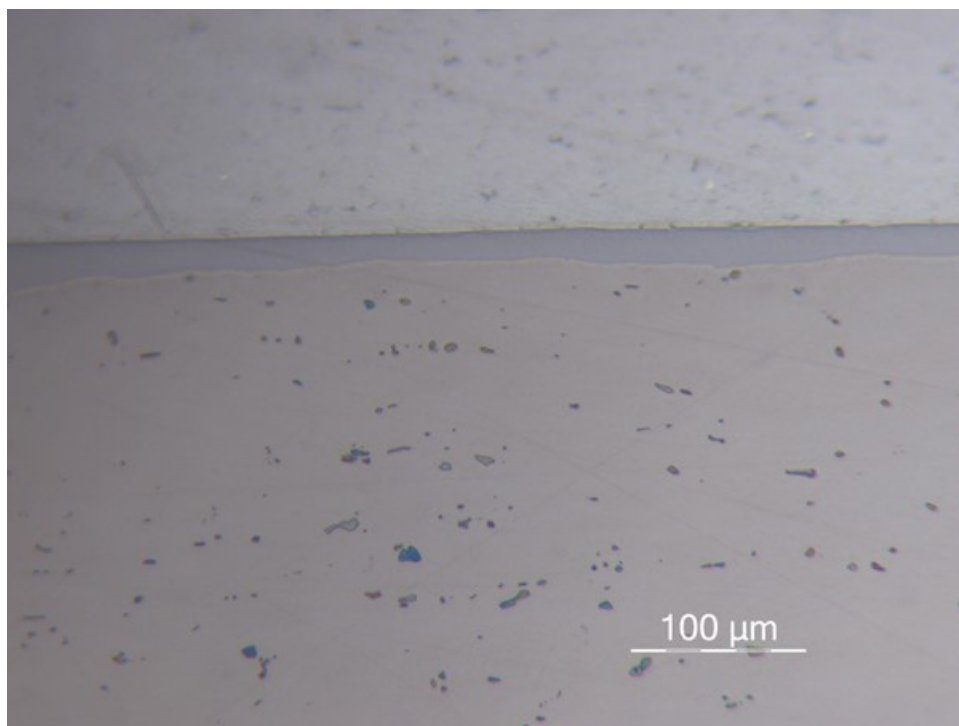


Figure 35. High magnification image of U-Mo/Zr/Al interface at plate midline. Fission density $\sim 2.7\text{E}+21$ fissions/cm³.

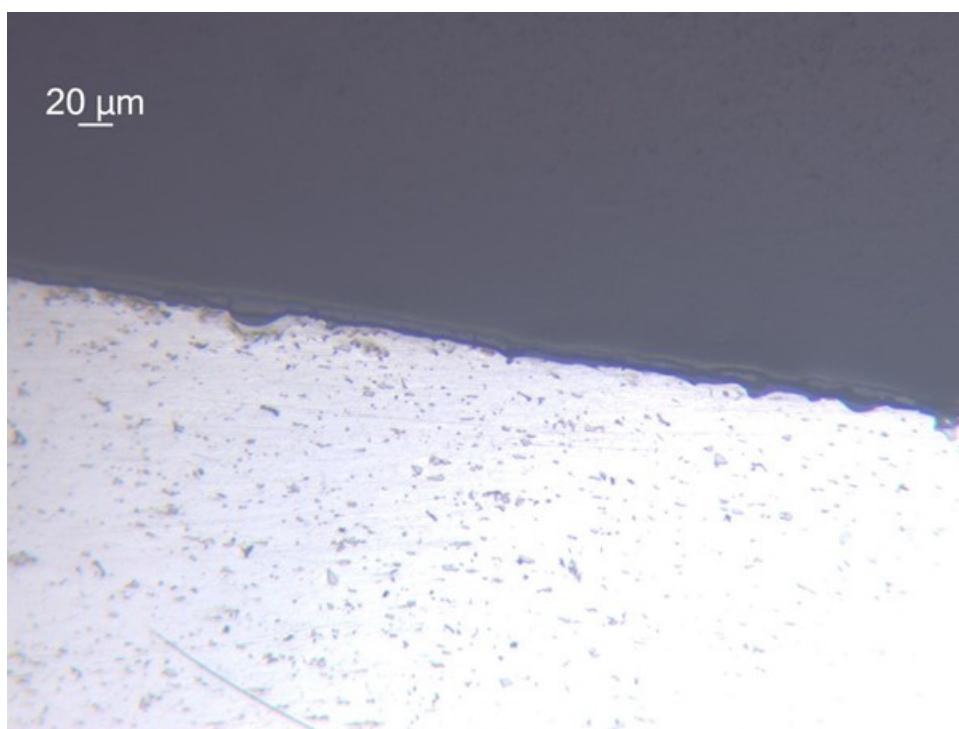


Figure 36. Image of oxide layer on plate ZH2 at plate mid line.

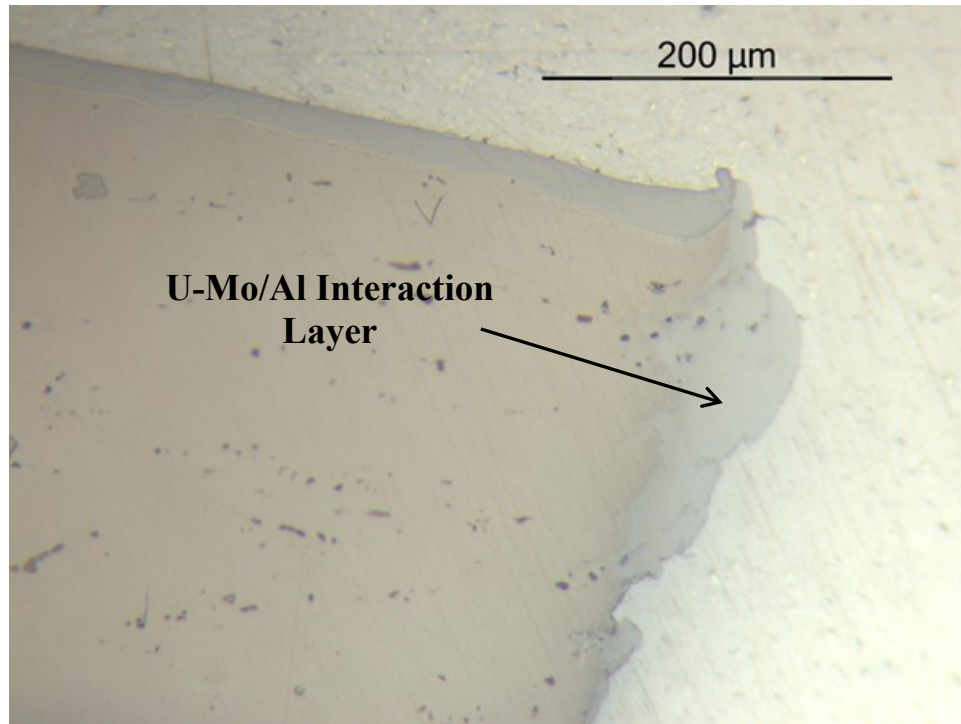


Figure 37. Image of ZH2 foil end at bottom of fuel zone. Fission density $\sim 2.0\text{E}+21$ fissions/cm³.

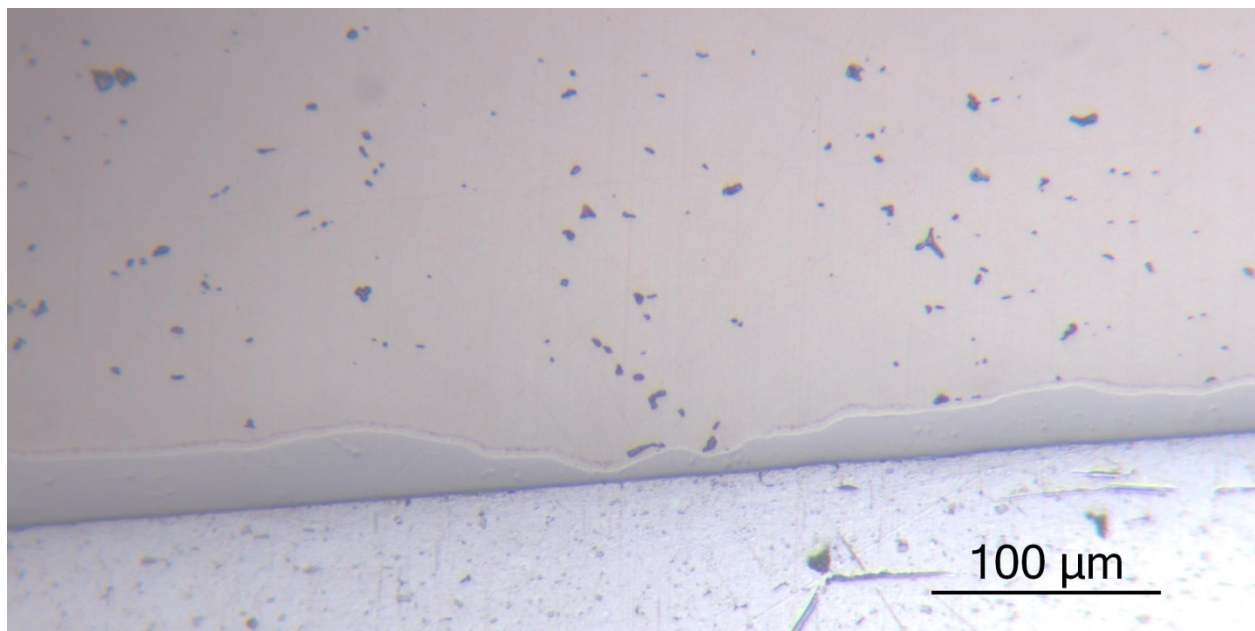


Figure 38. Image of region with thin zirconium diffusion barrier. Fission density $\sim 2.0\text{E}+21$ fissions/cm³.

4.1.2 Plate ZH4

4.1.2.1 Montages

Low magnification optical metallography samples from plate ZH4 are provided below. This includes the cross sectional samples prepared at the top of the plate, mid plane of the plate and bottom as well as the longitudinal samples from the bottom third of the plate.

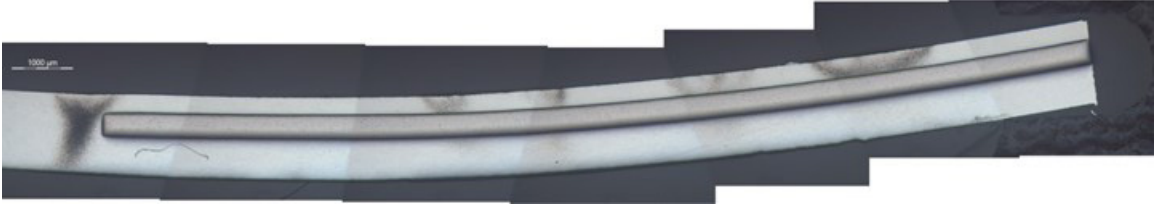


Figure 39. Metallography image 0.63 cm from top of fuel zone. Fission density $\sim 1.3\text{E}+21$ fissions/cm³.

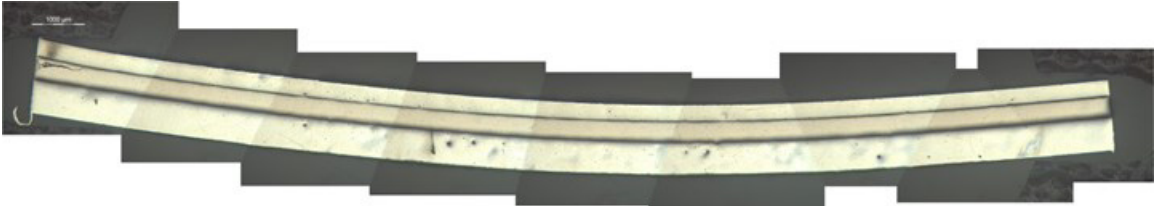


Figure 40. Metallography image 0.63 cm from top of fuel zone. Fission density $\sim 1.3\text{E}+21$ fissions/cm³.

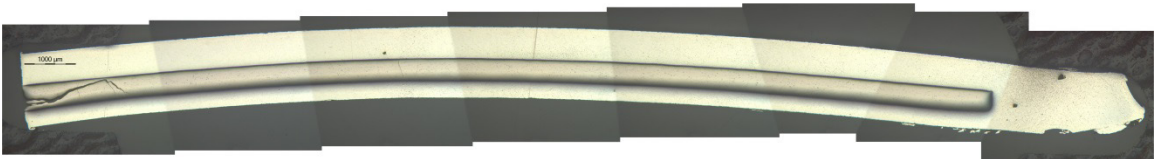


Figure 41. Metallography image from plate mid line. Fission density $\sim 2.8\text{E}+21$ fissions/cm³.



Figure 42. Metallography image from plate mid line. Fission density $\sim 2.8\text{E}+21$.

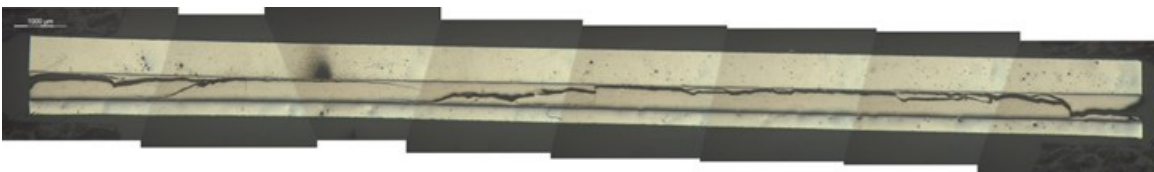


Figure 43. Longitudinal metallography sample from 28 cm from bottom of fuel zone. Fission density $\sim 2.8\text{E}+21$ fissions/cm³.

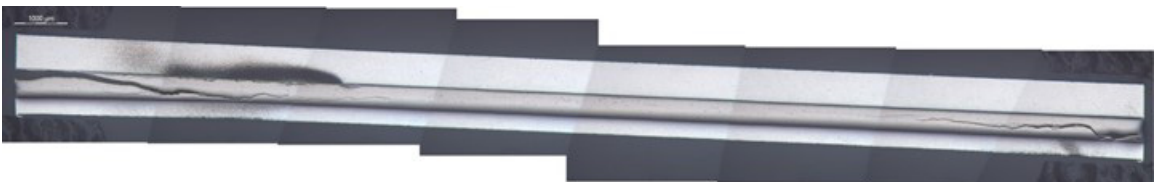


Figure 44. Longitudinal metallography sample from 28 cm from bottom of fuel zone. Fission density $\sim 2.8\text{E}+21$ fissions/cm³.



Figure 45. Metallography image 7 cm from bottom of fuel zone. Fission density $\sim 2.0\text{E}+21$ fissions/cm³.

4.1.2.2 High Magnification Images

Select, representative high magnification images of plate ZH4 are provided below. Images include regions from the uncovered edge of the fuel foil, U-Mo/Zr/Al interface regions, plate surface images and regions of interest of the fuel foil. Figure 50 through Figure 52 show an unexpected inclusion phase within one of the samples from plate ZH4. This was found in one of the longitudinal samples taken from the lower portion of the plate. The phase was several mm in length and up to 120 microns in thickness and appeared to contain multiple phases. Further discussion is provided in section 5.

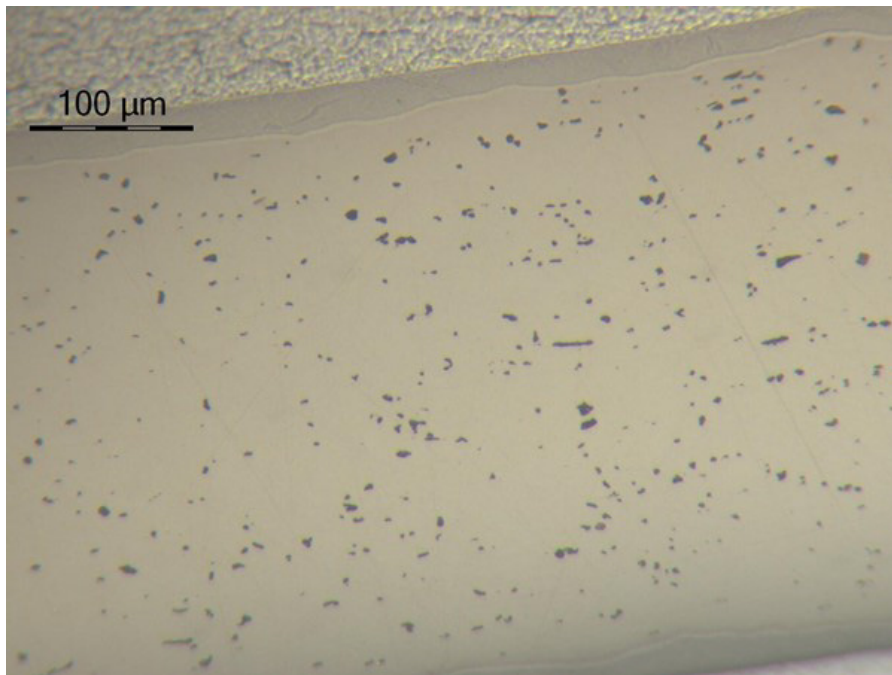


Figure 46. High magnification image of ZH4 fuel foil 0.63 cm from top of fuel zone. Fission density $\sim 1.3\text{E}+21$ fissions/cm³.

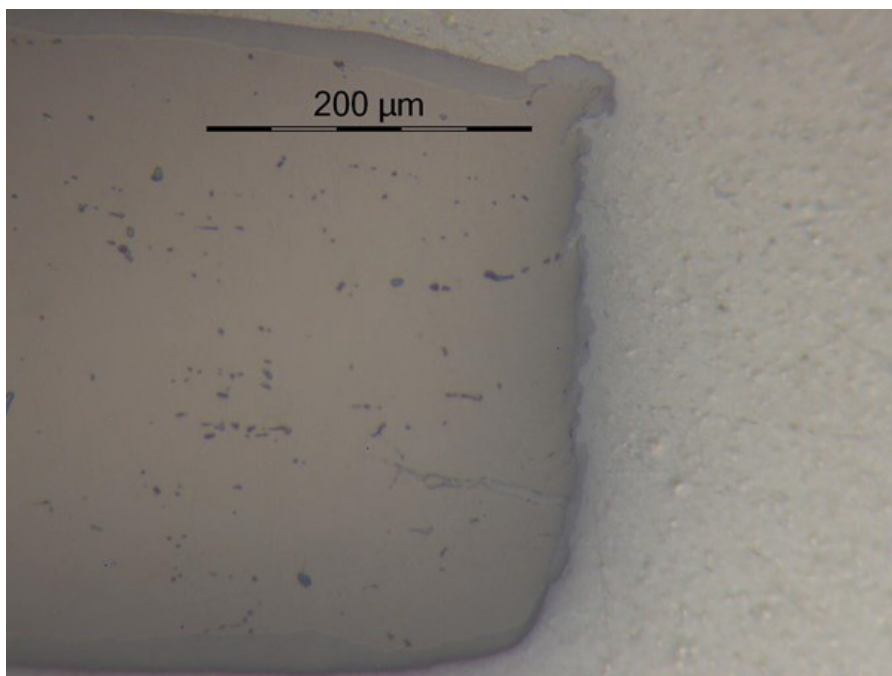


Figure 47. Image of ZH4 fuel foil end at plate mid plane. Fission density $\sim 2.8\text{E}+21$ fissions/cm³.

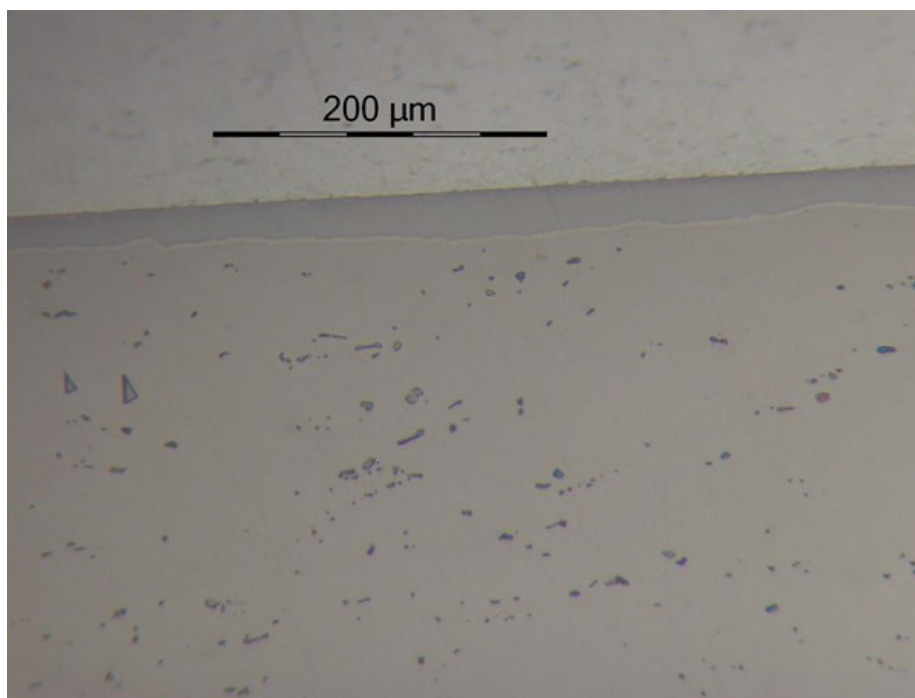


Figure 48. Image of U-Mo/Zr/Al interface at plate mid plane. Fission density $\sim 2.8\text{E}+21$ fissions/cm³.

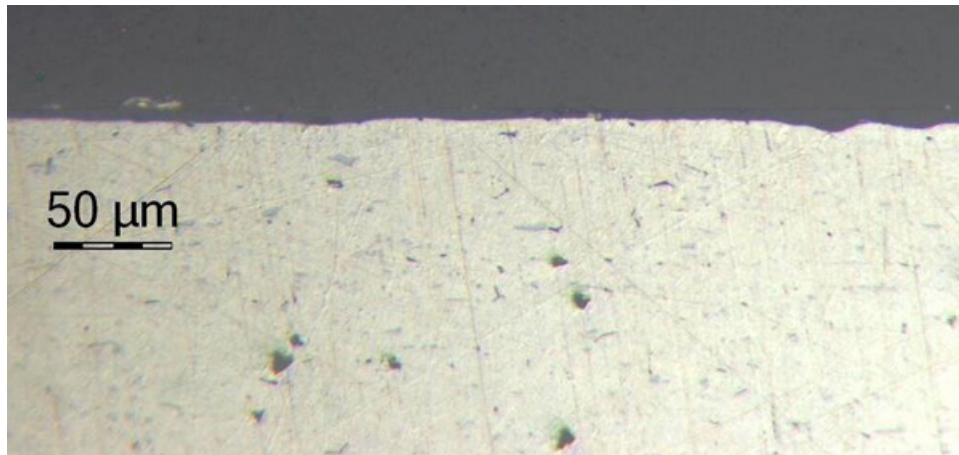


Figure 49. Image of oxide layer formed on plate ZH4.

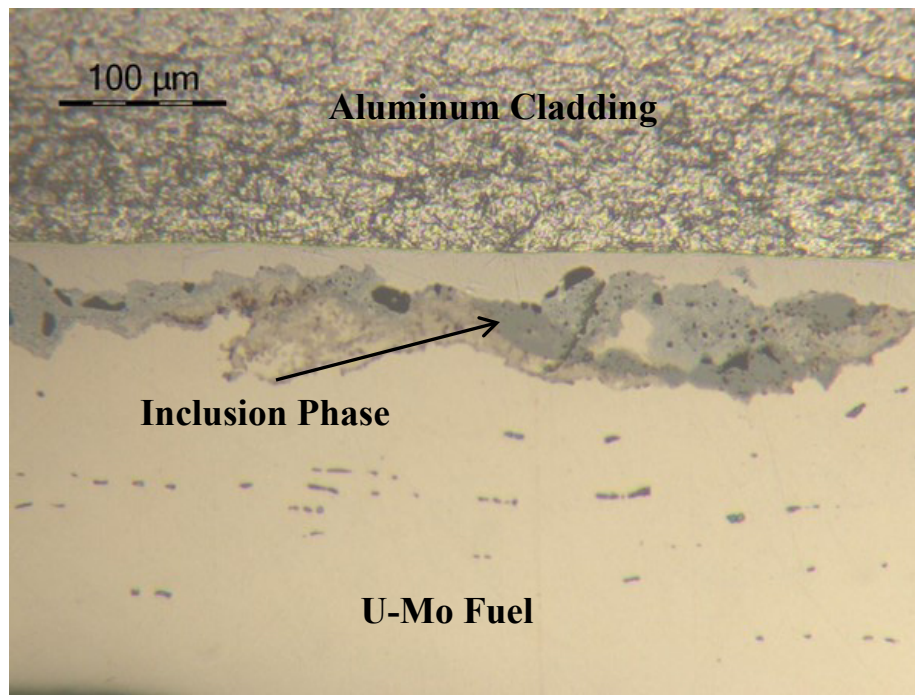


Figure 50. Image of inclusion phase in ZH4 fuel foil 28 cm from bottom of fuel zone.

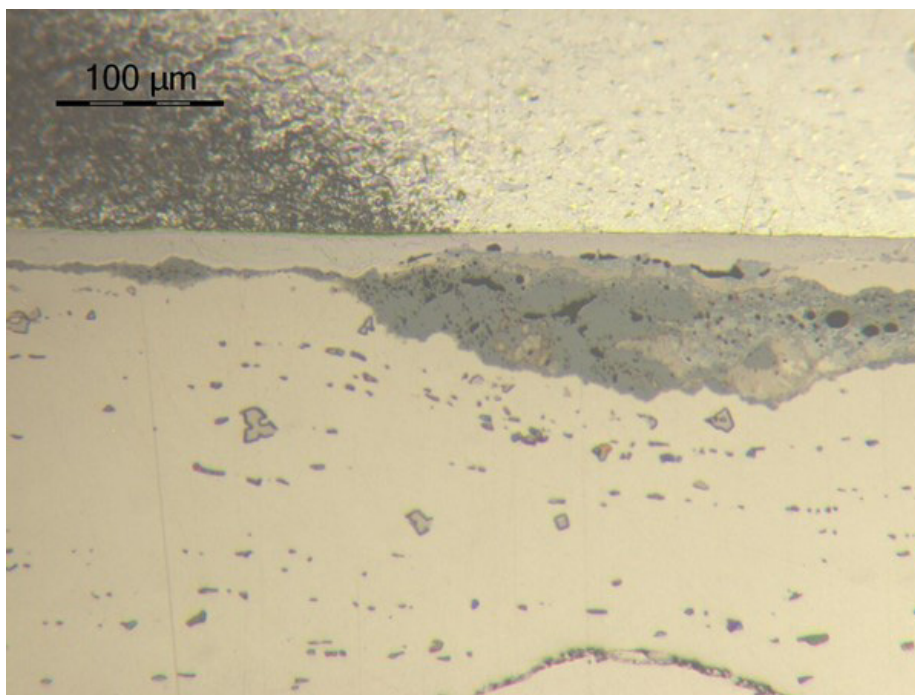


Figure 51. Image of inclusion phase in ZH4 fuel foil.

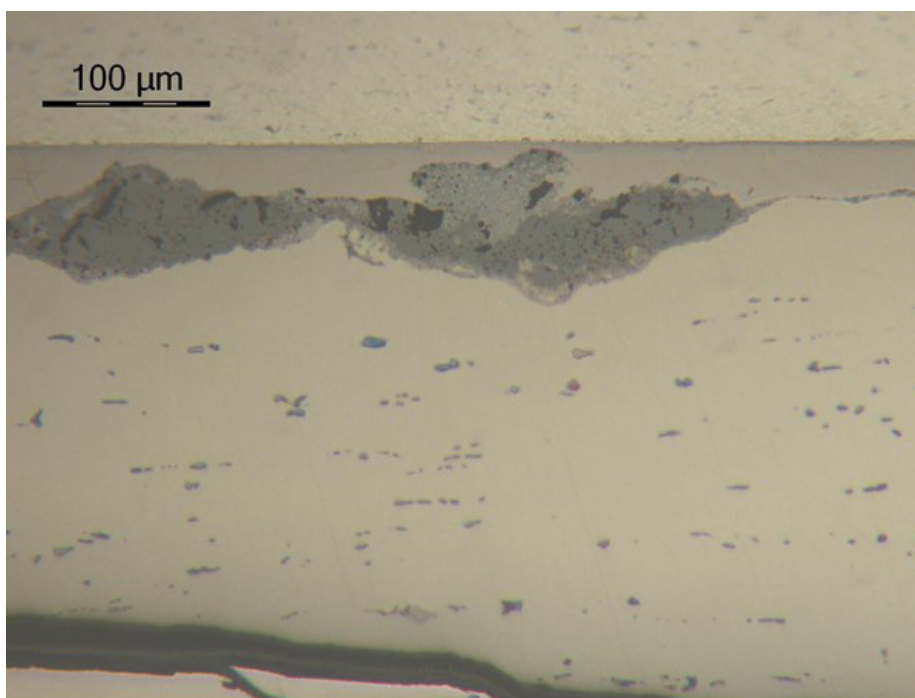


Figure 52. Image of inclusion phase in ZH4 fuel foil.

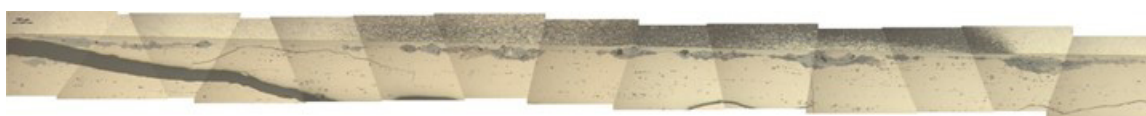


Figure 53. Montage of region with inclusion phase in ZH4 fuel foil.

4.2 Chemical Burn-up Analysis

Samples were collected from plates ZH2 and ZH4 to perform chemical burn-up analysis. Four 6.35 mm wide cross-sectional samples were taken from each of the plates that can be compared directly with longitudinal regions where neutronic (MCNP) calculations were performed. Two samples were taken from the top portion of each plate, one from the center region of each plate, and one from the lower region of each plate. In addition, two cross sectional samples from each plate were sub-sized to quantify transverse burn-up. Each of the two samples was sectioned into two 6.35 mm wide slices at the foil edge, and two 25.4 mm slices from the center region of the plate. See Figure 25 for sectioning locations. Samples were then transferred to the analytical laboratory hot cells for analysis.

Upon receipt of the samples, they were weighed, dissolved, and the resultant solutions were analyzed for uranium, plutonium and selected fission-product isotopes using inductively coupled plasma mass spectrometry (ICP-MS). Total uranium as well as uranium isotopes analyzed includes U₂₃₄, U₂₃₅, U₂₃₆, and U₂₃₈. Total plutonium as well as plutonium isotopes analyzed include Pu₂₃₉, Pu₂₄₀, Pu+Am₂₄₁ (includes americium-241), and Pu₂₄₂.

Table 3. ICP-MS results for each sample used to calculate depletion

	234U	235U	236U	238U	U Total		239Pu	240Pu	241M/z	242Pu	Pu Total
Sample ID	(ug/g)	(ug/g)	(ug/g)	(ug/g)	(ug/g)		(ug/g)	(ug/g)	(ug/g)	(ug/g)	(ug/g)
1664	1020	84700	4530	433000	523250		1850	160	43.2	2.05	2055
2274	1080	81700	5480	444000	532260		2190	226	76.7	4.3	2497
2275	962	60800	8970	440000	510732		3090	540	288	36	3954
2276	553	37700	6180	301000	345433		2170	404	213	30.3	2817
2277	919	64400	8930	456000	530249		3320	570	300	37.5	4228
2278	946	64100	9180	450000	524226		3300	564	304	37.6	4206
2279	768	44200	7500	345000	397468		2630	495	268	39.1	3432
2280	683	44400	5070	292000	342153		1970	293	122	12.3	2397
2281	1080	77800	6910	459000	544790		2800	365	154	11.8	3331
2282	980	71600	6460	429000	508040		2600	336	141	11.7	3089
2284	718	47000	5210	302000	354928		1920	283	123	11.3	2337
2285	1050	77000	7060	460000	545110		2670	348	143	11.5	3173

4.3 Blister Threshold Testing

Out-of-pile post-irradiation blister threshold testing has been conducted historically to provide data that is used in reactor safety analyses to provide a conservative margin for the fuel operating temperature limits under normal operating conditions and anticipated transients. Fuel blistering can cause geometry changes that result in a loss of coolability (e.g. channel-gap closure) and is also considered a precursor to fuel failure involving cladding breach that can result in fission product release.

The blister threshold test involves furnace heating the plates in an out-of-pile test conducted in the hot cell. Blister testing for the AFIP-7 plates was performed in the new large blister anneal furnace in the Hot Fuel Examination Facility.¹⁰ This system is capable of blister threshold testing full-size (ATR type) fuel plates. A specimen is held at an elevated temperature for a period of time and then removed from the furnace and visually examined for the presence of blisters. If no blister is observed, the specimen is returned to the furnace for the next anneal cycle at an incrementally higher temperature setting. This process is repeated until a blister is observed.

Two AFIP-7 plates, 7ZH1 and 7ZH3, were blister threshold tested. Information regarding the tested plates can be seen in Table 4. Both plates formed blisters on the plate surface at 475 degrees C.

Table 4 AFIP-7 Blister threshold test specimens with pertinent irradiation conditions

Plate	Average fissions/cm³ (10²¹)	Peak fissions/cm³ (10²¹)	Fission power density (W/cm³)	Blister threshold temperature (°C)
7ZH1	2.28	2.68	7.86E+03	475
7ZH3	2.25	2.61	7.86E+03	475

The blistered regions of 7ZH1 front and back are shown in Figure 54 and Figure 55 respectively. The blistered region of plate 7ZH1 shown in Figure 4 shows different blistering behavior than historically seen for monolithic type fuel. Typical blistering behavior for monolithic fuel plates are blisters along fuel edges. Plate 7ZH1 has blisters that have formed across the width of the plate. One hypothesis for this is the impurities phase between the zirconium diffusion barrier interlayer and the U-10Mo fuel foil seen in optical metallography. These impurities may serve as nucleation sites for fission gas coalescence. Another hypothesis is that improved fabrication techniques have improved the bond strength between the U-Mo fuel and zirconium interlayer and improved fuel foil edge behavior resulting in many small blisters more typical of dispersion type fuel. Metallographic examination of the blister annealed test plates is recommended of these unexpected results.

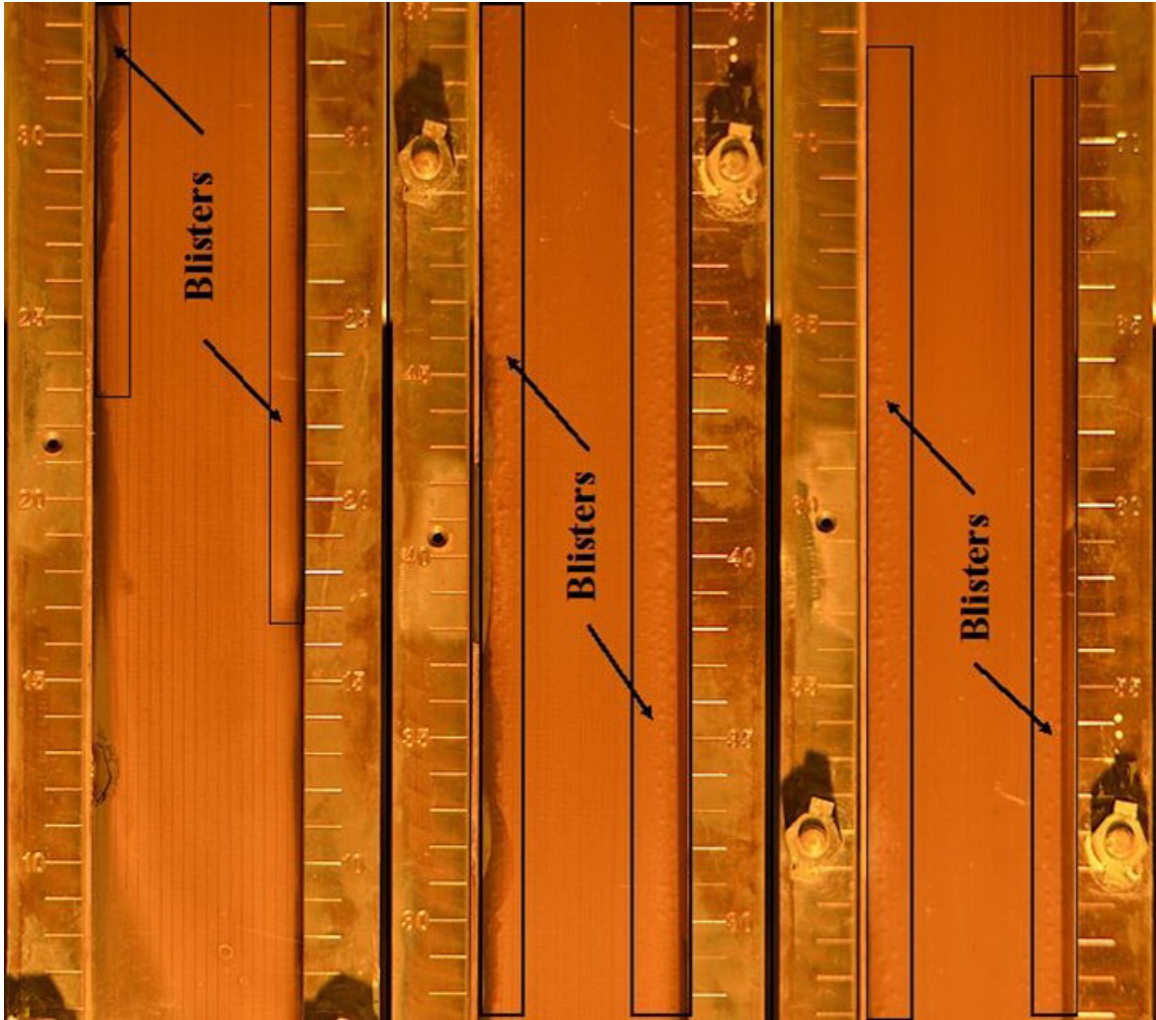


Figure 54. AFIP-7 plate 7ZH1, front side, showing blistered region of plate.

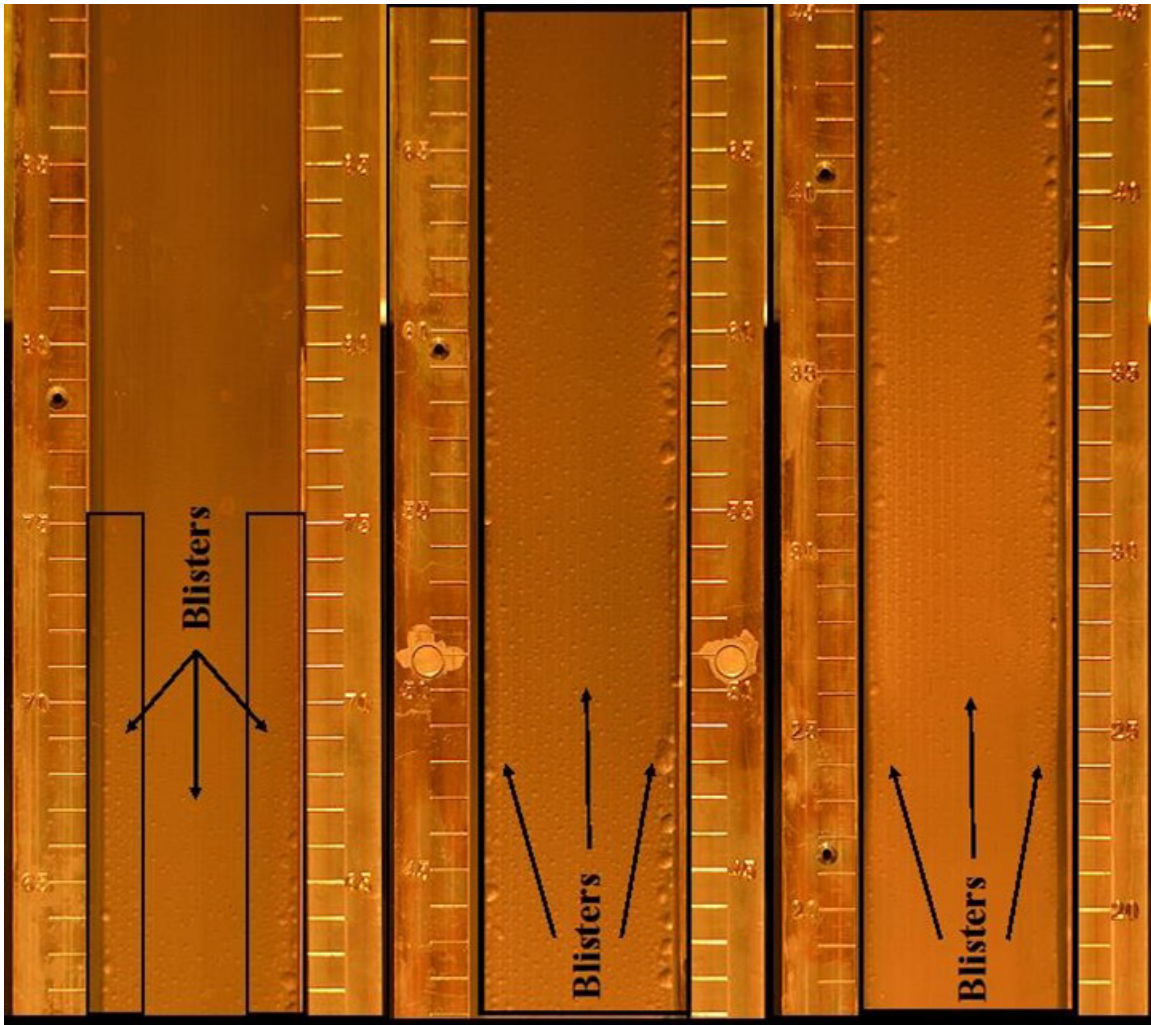


Figure 55. AFIP-7 plate 7ZH1, back side, showing blistered region of plate.

Plate 7ZH3 front and back blistered regions are shown Figure 56 and Figure 57 respectively. The blister formation behavior for this plate was more typical of what has previously been observed during blister threshold testing of monolithic fuel plates, where blisters have formed primarily along fuel foil edges.¹¹

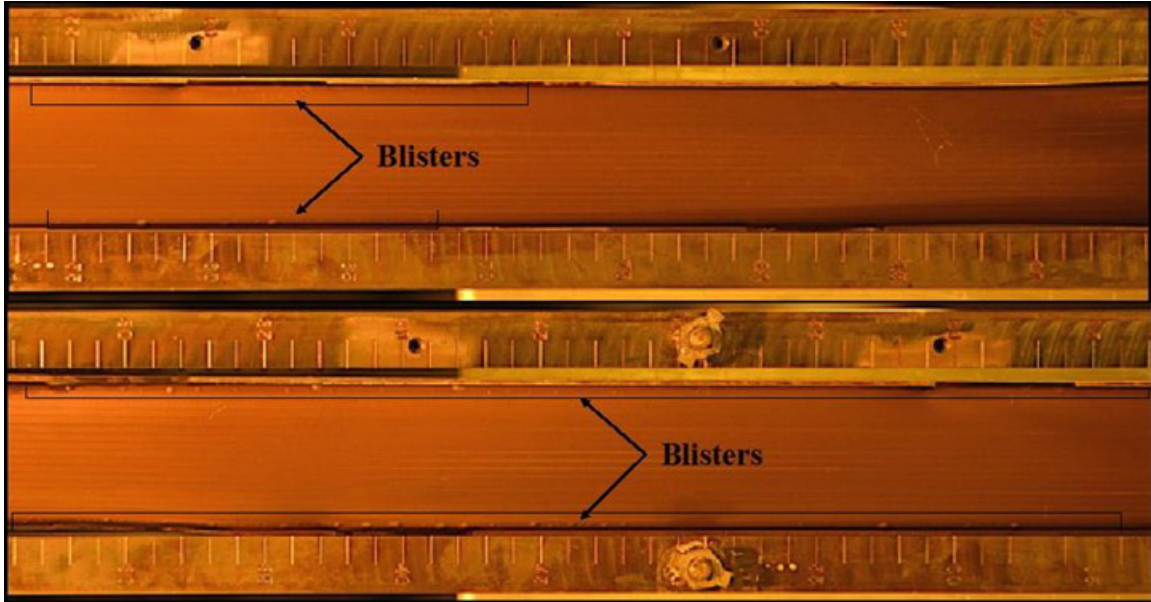


Figure 56. AFIP-7 plate 7ZH3, front side, showing blistered region of plate.

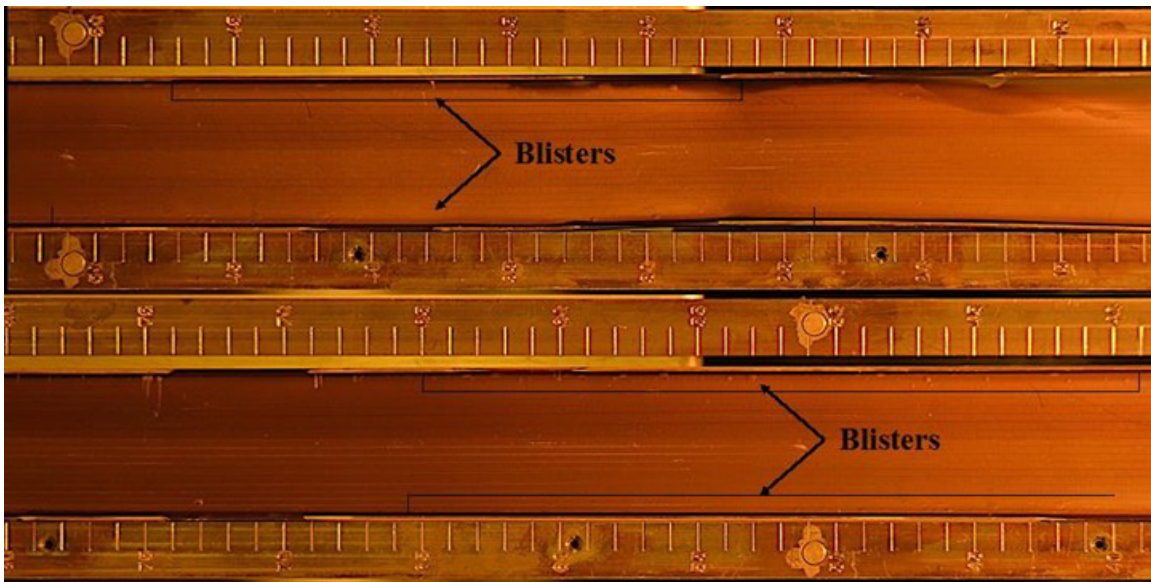


Figure 57. AFIP-7 plate 7ZH3, back side, showing blistered region of plate.

Figure 58 and Figure 59 show the AFIP-7 blister threshold temperatures as a function of plate average and plate peak fission densities, respectively. The AFIP-7 and AFIP-4 (all the scale-up plates blister threshold tested to date) are indicated by green circles (with AFIP-7 highlighted) are nested within the trend model and respective confidence intervals, also shown in green. These results show the AFIP-7 plates behaved as expected, well within the individual 95% confidence bounds for the mini-plate data and near the mini-plate prediction value based on the AFIP-7 fission density.

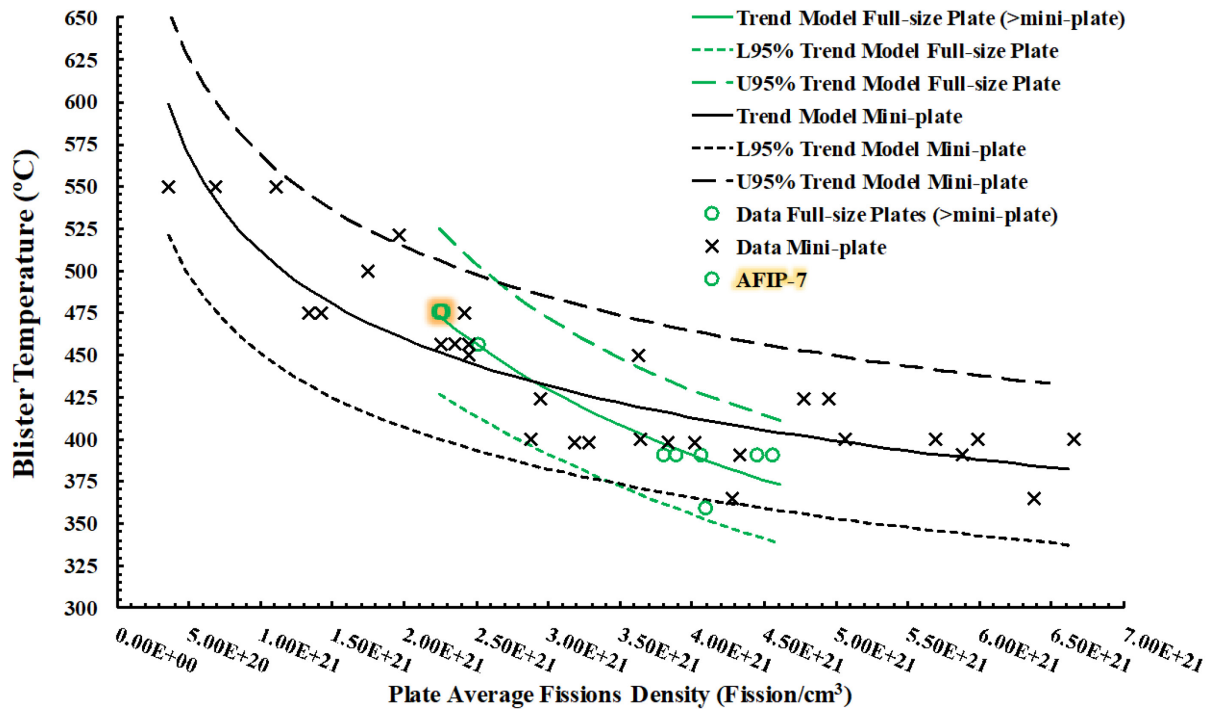


Figure 58. AFIP-7 blister threshold results versus average fission density with historical data from previous monolithic blister threshold tests and the 95% upper and lower confidence intervals.

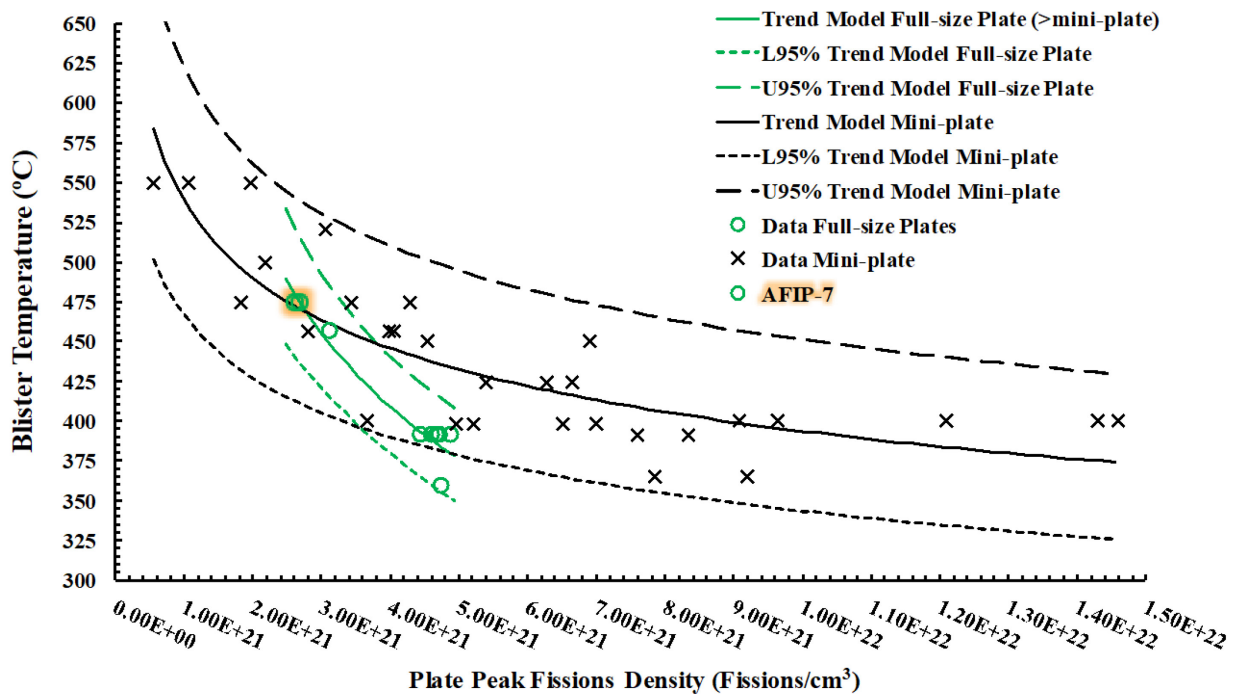


Figure 59. AFIP-7 blister threshold results versus plate peak fission density with historical data from previous monolithic blister threshold tests and the 95% upper and lower confidence intervals.

5. DISCUSSION

Visual examination and neutron radiography did not provide any indication that any of the four AFIP-7 plates behaved in an unexpected manner. Visual examination showed that the plates appeared mechanically sound with no twisting, bowing, warping or blistering. Radiography did not show any unusual phenomenon related to the fuel within the plate. No cracking or fuel relocation was observed. The foreign substance observed at the bottom of the plate was the only item of note from the initial inspection. This substance impacted the thickness and eddy current data collection at the bottom of the plates but did not hamper any other examinations.

Using the isotopic values from the chemical analysis, U-235 burn-up values can be calculated for each sample. Burn-up values were calculated for each sample using Equation 1. This equation uses the beginning of life U_{235}/U_{238} ratio, and the end of life U_{235}/U_{238} ratio accounting for the neutron capture of U_{235} to U_{236} as well as the neutron capture of U_{238} to Pu to calculate the burned U_{235} atoms. The sample information, MCNP calculated burn-up and fission density, and the chemistry measured burnup along with a comparison of the values is shown in Table 5.

Equation 1 U-235 burn-up equation

$$U - 235 \text{ Burnup} = \frac{\left[\frac{(U_{235})}{(U_{total})} \right]_{BOL} - \left[\frac{(U_{235} + U_{236})}{(U_{total} + PU_{total})} \right]_{EOL}}{\left[\frac{(U_{235})}{(U_{238})} \right]_{BOL}}$$

Table 5 Chemical analysis results compared to calculated values

Sample ID	Description	Longitudinal location [cm]	Calculated Burnup	Calculated Fission Density	L2AR	Local Calculated Burnup	Local Calculated Fission Density	Local Measured Burnup	Difference
1664	Cross section from top of foil	2.54	21.55	1.48E+21	1.00	21.55	1.48E+21	17.18	23%
2274	Cross section from top of foil	7.62	25.47	1.76E+21	1.00	25.47	1.76E+21	21.16	18%
2275	Cross section from centerline	44.45	37.45	2.67E+21	1.00	37.45	2.67E+21	36.54	2%
2276	left edge at centerline	49.53	36.98	2.63E+21	1.13	41.79	2.97E+21	41.68	0%
2277	left-center at centerline	49.53	36.98	2.63E+21	0.98	36.24	2.58E+21	35.66	2%
2278	right-center at centerline	49.53	36.98	2.63E+21	0.98	36.24	2.58E+21	34.86	4%
2279	right edge at centerline	49.53	36.98	2.63E+21	1.10	40.68	2.89E+21	40.09	1%
2280	left edge from bottom of foil	92.71	27.94	1.95E+21	1.10	30.73	2.15E+21	32.15	5%
2281	left-center from bottom of foil	92.71	27.94	1.95E+21	0.98	27.38	1.91E+21	26.02	5%
2282	right-center from bottom of foil	92.71	27.94	1.95E+21	1.00	27.94	1.95E+21	27.05	3%
2284	right edge from bottom of foil	92.71	27.94	1.95E+21	1.17	32.69	2.28E+21	30.73	6%
2285	cross section from bottom of foil	93.98	26.93	1.95E+21	1.00	26.93	1.95E+21	26.72	1%

Gamma scanning of the fuel plates all showed uniform fission product distribution that matched calculated profiles. No fission product migration or unusual peaking was seen. To support verification of calculated MCNP values, the relative gamma scans can be scaled using the experimentally measured chemical burn-up values tabulated above. By scaling the longitudinal gamma scans, a longitudinal burn-up profile of all four plates can be created. The profiles can be seen in Figure 60.

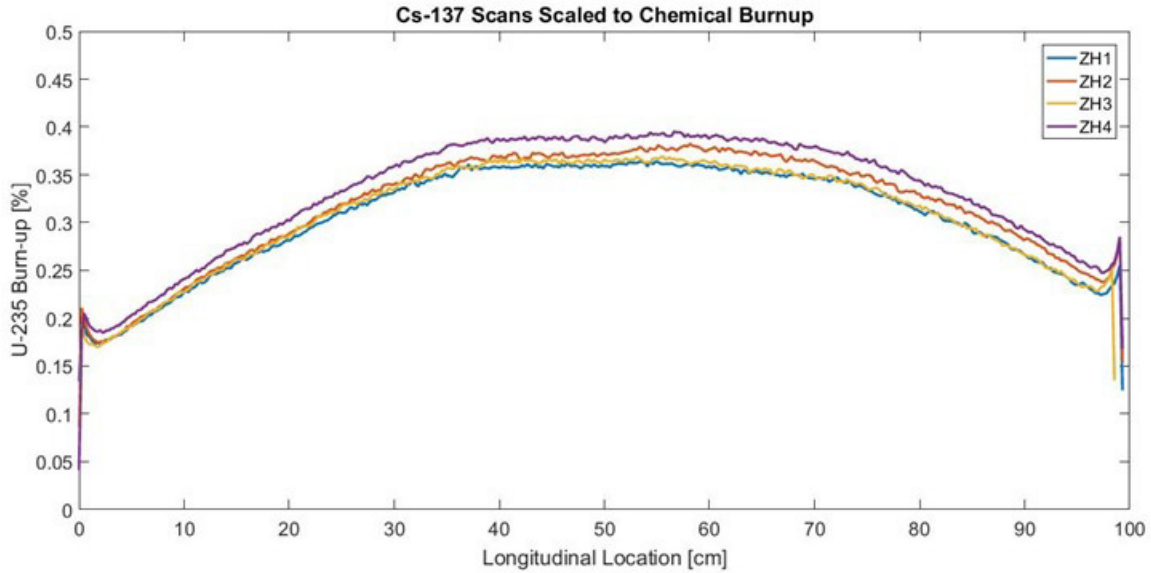


Figure 60. Longitudinal gamma scans scaled to experimentally measured chemical burn-up.

The longitudinal and transverse gamma scans were combined and used to build a relative two-dimensional fission density profile over the plates. This two dimensional profile was then multiplied into the calculated plate average values for fission density, power, and surface heat flux to create surface profiles for each of the fuel plates. The completed two dimensional fission density map for each plate is shown in Figure 61. Comparing the profile of the fission density determined from scaling the gamma scan data with the MCNP calculated fission density profile, as shown in Figure 8, the measured and calculated fission density profiles appear to be very similar. Peak fission densities occur on the edges of the plate near the mid plane, as expected, and the calculated L2AR values appear to be reasonable.

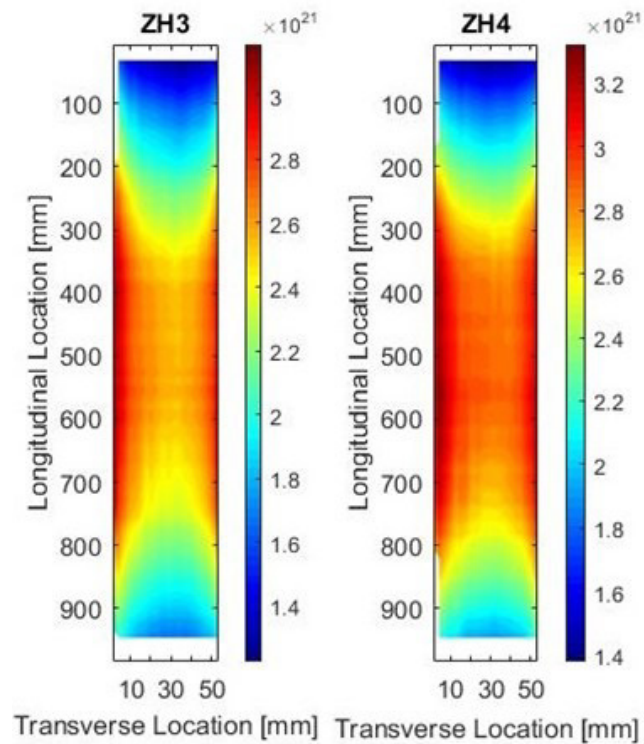
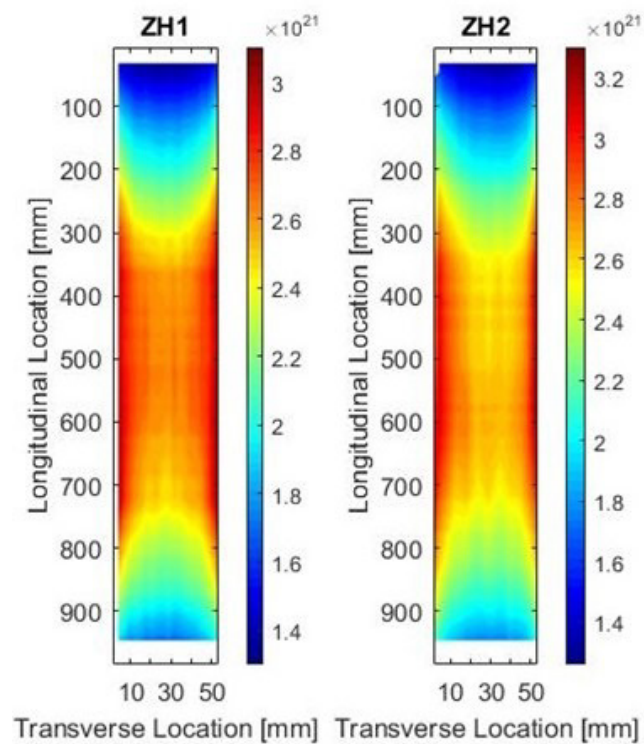


Figure 61. Fission density plots determined by scaling the gamma scan data.

Using the location specific burn-up values to scale the relative longitudinal gamma scans, measured longitudinal burn-up profiles can be created. Using the measured burn-up profiles to compare with the calculated fission density profiles down the length of all four plates, good agreement can be seen for the majority of the experiment, Figure 62. The measured versus calculated profiles are in close agreement with the exception of the top portion of the plates. The measured profiles indicate a steeper gradient of the fission density existed than was captured in the calculated values for the top 20 cm for plates ZH1, ZH2 and ZH3 and the top 35 cm for plate ZH4. The reason for this discrepancy is not known at this time and it is recommended that this be investigated further.

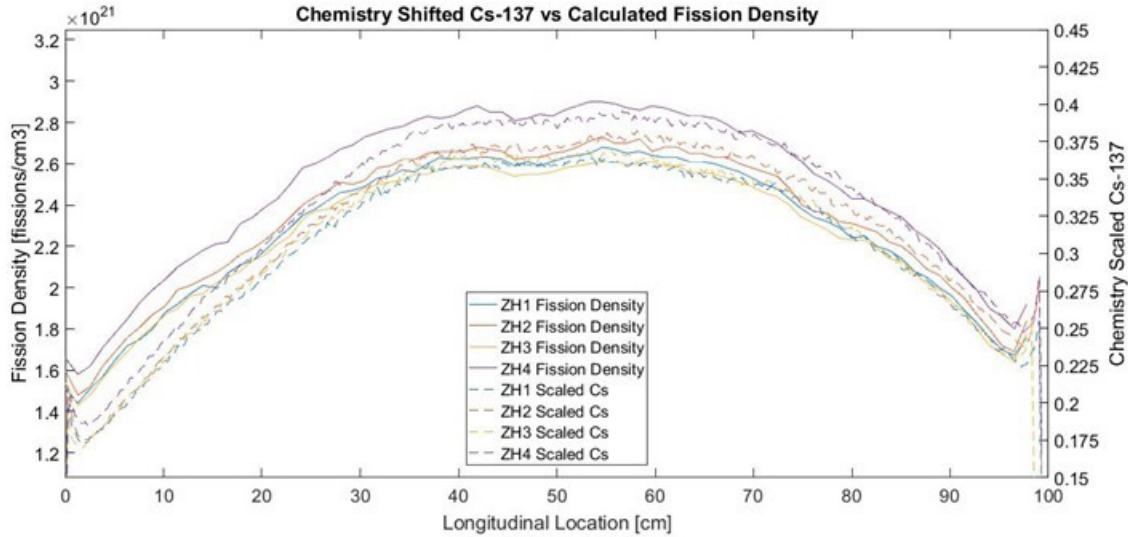


Figure 62. Chemical burn-up scaled gamma scans compared to calculated fission density profiles.

Thickness measurements indicated uniform fuel behavior with peak thicknesses occurring at the highest fission density locations. In order to directly compare the performance of the AFIP-7 plates with other similar experiments using a different fuel design (i.e. fuel loading or plate geometry, etc.), the swelling is typically expressed in terms of ‘fuel phase swelling’, or simply ‘fuel swelling’. In this representation, all of the fuel plate growth is attributed to the fuel phase only and is defined as the change in fuel plate volume divided by the original fuel phase volume. This assumption is reasonable to the first order but ignores density changes due to interaction product formation, irradiation induced swelling of the interaction product, cladding swelling, and fuel microstructural changes due to irradiation effects beyond fission product-induced swelling. In some cases, specific factors that contribute to fuel plate swelling can be isolated and corrections to calculations can be made. In the case of AFIP-7, a correction for oxide layer formation is performed.

The plate thickness is converted into the local volume change using Equation 2.

Equation 2 Fuel phase swelling calculations

$$G_f = \frac{\left(t_p - \frac{1}{1.975} t_{ox}\right) - t_{p0}}{(t_f - t_{Zr})V_f}$$

where G_f is the fuel phase growth, t_p is the local plate thickness measured post irradiation, t_{ox} is the local surface oxide thickness, t_{p0} is the pre-irradiation local plate thickness, t_f is the initial fuel foil thickness, t_{Zr} is the nominal zirconium diffusion layer thickness and V_f is the as-fabricated fuel volume fraction in the fuel meat ($V_f=1$ in monolithic fuels such as AFIP-7).

The resulting calculated two-dimensional fuel swelling profiles for each plate can be seen in the contour plots in Figure 63. As expected, the peak swelling regions occur at the edges of the plates near the center longitudinal positions. These plots correlate well to the fission density profiles shown in Figure 61.

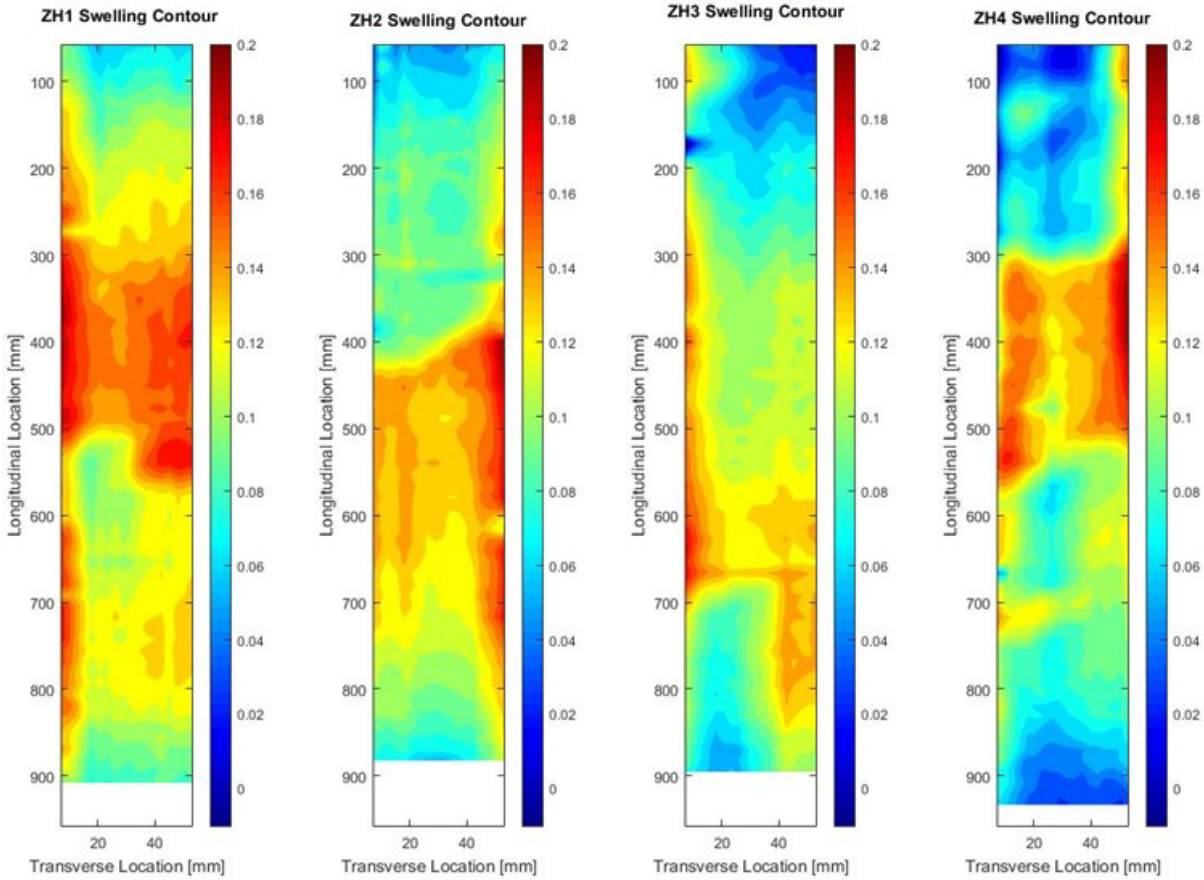


Figure 63. Fuel swelling contour of all AFIP-7 plates.

The plate thickness measurement grid and subsequent fuel swelling grid resolution is considerably higher than the calculated fission density profile. Therefore, in order to correlate local measured fuel swelling with local calculated fission density, the fuel swelling values are averaged down to a common grid. This results in approximately 20 thickness values contributing to each reported fuel swelling value. The fuel local measured swelling as a function of local calculated fission density for each plate is shown in Figure 64. The fuel swelling correlation developed by Kim and Hofman using historical U-Mo data is plotted for reference.¹²

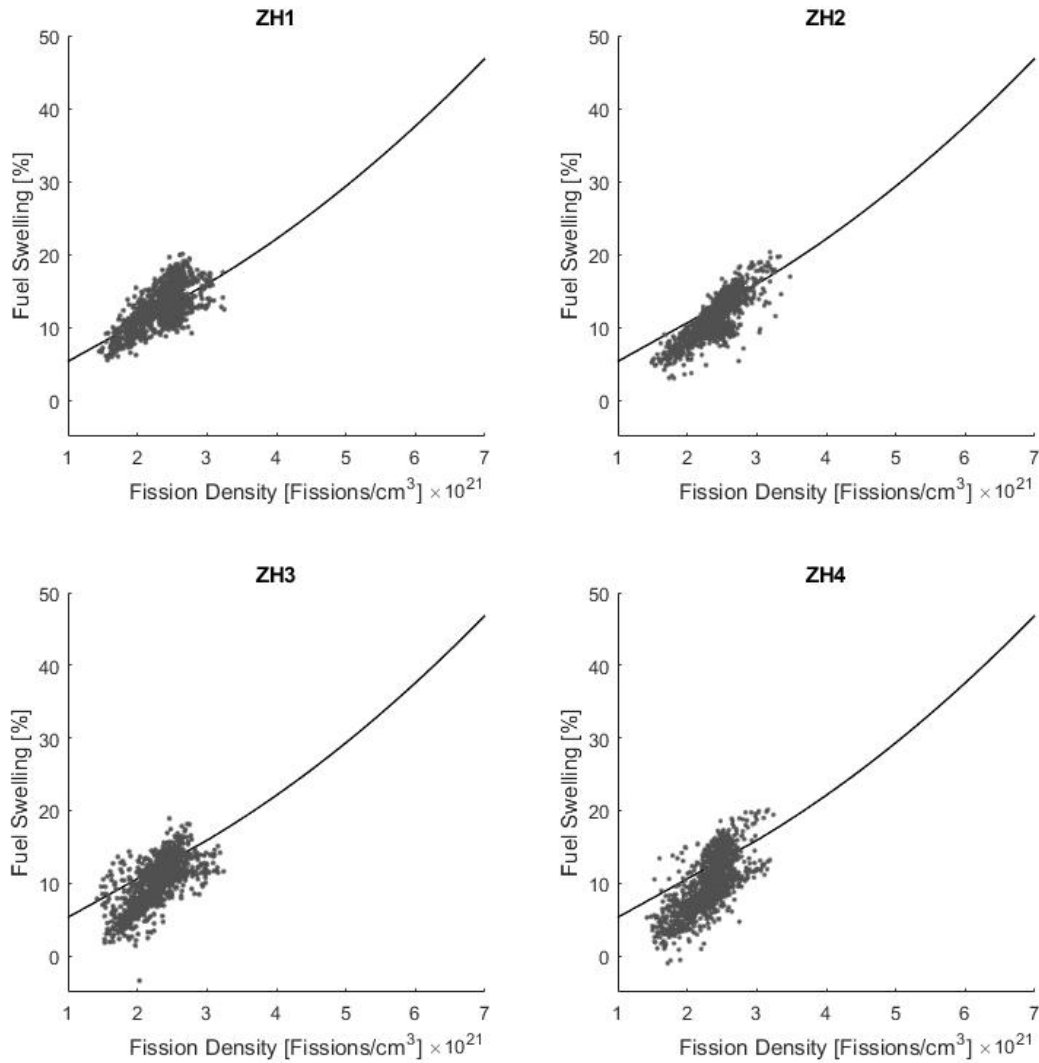


Figure 64. AFIP-7 fuel swelling versus fission density with Kim and Hoffman swelling correlation.

In order to account for the uncertainties in local variations in fuel swelling due to geometric effects (fuel edges, fuel creep, etc.), pre-irradiation foil thickness variations, and uncertainties in the local calculated fission density values, the calculated fuel swelling values are ‘binned’ according to fission density. In the present analysis, all swelling data falling within bins having a width of 0.1×10^{21} fissions/cm³ are averaged together into one data point. This is done using only the local calculated fission density and is independent of geometric location of the measurements on the plate. The binned data plotted as a function of fission density can be seen for each plate in Figure 65.

The binned fuel swelling data for all four AFIP-7 plates appears to be in reasonable agreement with the fuel swelling correlation. The fuel swelling for plate ZH1 appears to be slightly higher than the other plates but is within uncertainties in the calculations. Pre-irradiation thickness values for both the plates and foils are recorded to $\pm 25 \mu\text{m}$ significant digits (.001 inches) while post irradiation values are recorded at significant digits to $1 \mu\text{m}$. Variations of the plate and foil thicknesses below the reported accuracy of

the pre-irradiation thickness values are truncated (e.g., 0.0155 inches would be reported as 0.015 inches), therefore the calculated swelling can vary up to approximately 7%.

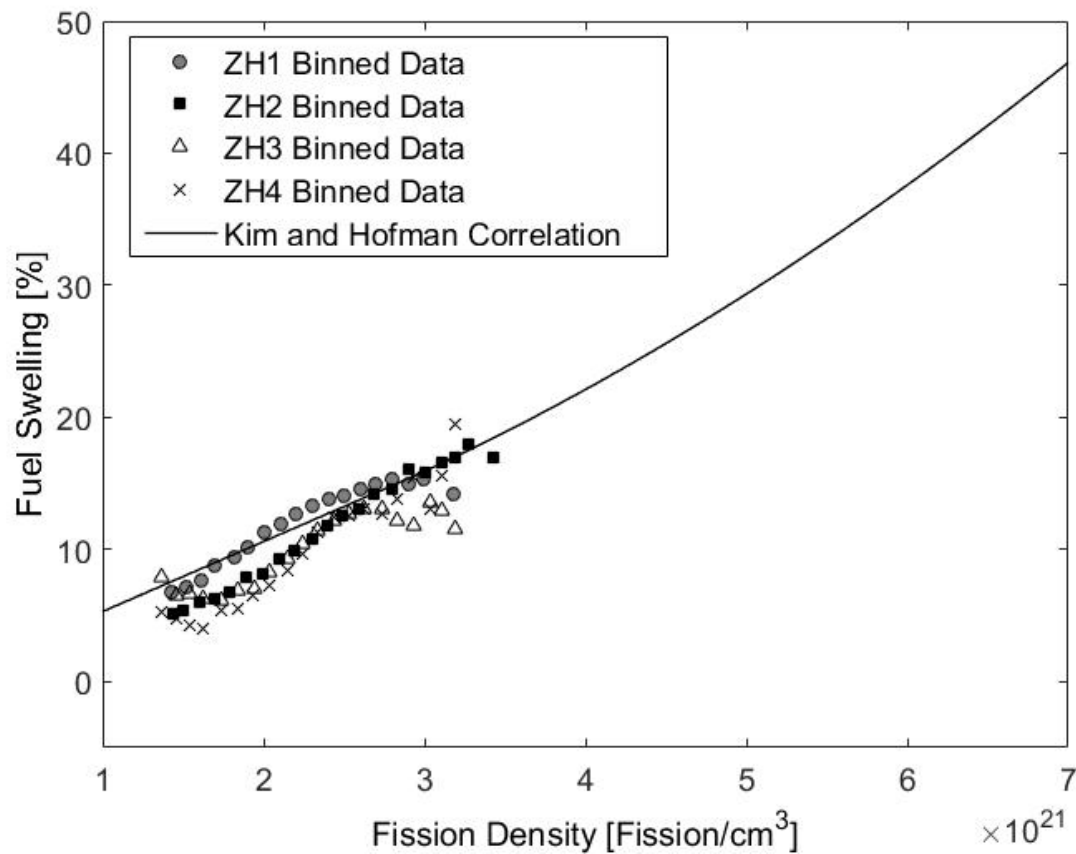


Figure 65. AFIP-7 binned swelling versus fission density for each plate with “Kim and Hofman, 2011” swelling correlation.

Statistical analysis of the binned swelling data was performed for each plate. For this analysis, a least squares trend line was created for each of the four plates, where the data points are weighted by the number of data points averaged into that point. A 95% confidence limit is then calculated for the trend line. The trend line and confidence limits for each plate are shown in Figure 66.

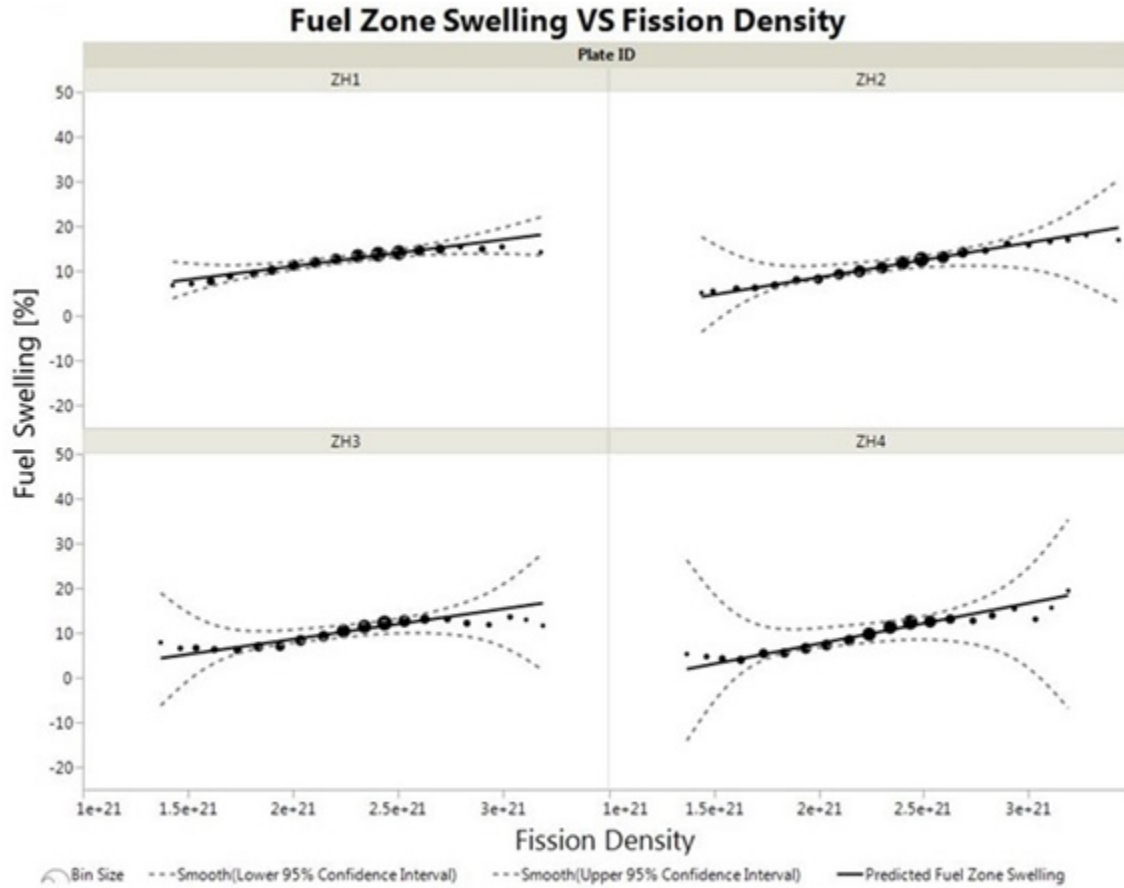


Figure 66. Least squares fit of binned swelling versus fission density with 95% confidence limits.

Taking the swelling versus fission density data for all four plates together and binning them, again into $0.1E21$ fission/cm³ step sizes, a trend line and confidence limits can be created for the entire AFIP-7 experiment. Figure 67 shows the entire fuel swelling data set, the binned data and a least squares fit with 95% confidence limits. The uncertainty increases at the high and low fission density values for the experiment due to the limited amount of data at the extremes, but the experiment trend line matches very well with the Kim and Hofman fuel swelling correlation.

All analysis of the fuel swelling presented here appears to indicate consistent behavior that is stable and predictable. While local variations exist, the extremely large set of high resolution grid measurements clearly demonstrates that the fuel is behaving as expected.

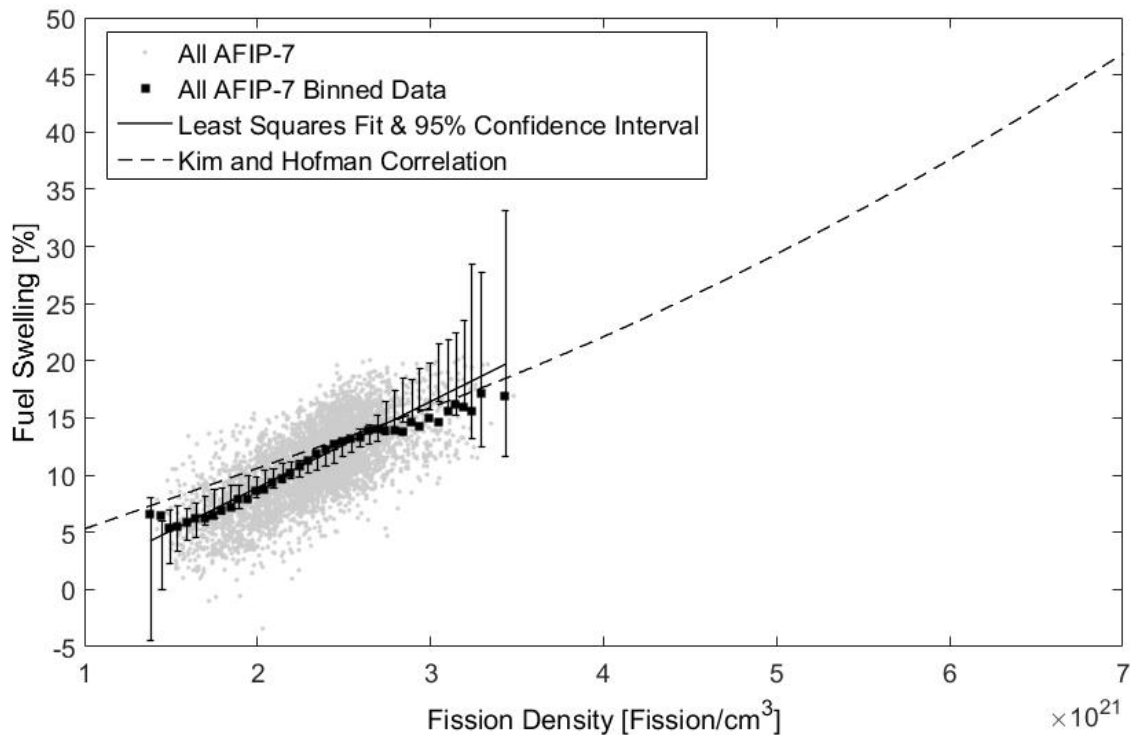


Figure 67. All AFIP–7 swelling versus fission density with fuel swelling correlation.

The AFIP–7 blister threshold temperatures are within the 95% confidence interval developed from the previous blister threshold trending data. Plate blistering regions are clearly correlated with regions of highest fission density (fissions/cm³) and plate power (W/cm³).

Trend models were evaluated for both mini-plates (largest data population) and scale-up plates (AFIP–4 and AFIP–7) and are shown in Figure 68. Note that the uncertainty increases at the beginning and at the end of the model for larger plates. The current trend indicates that following fission densities greater than 3.5E+21 fissions/cm³ the blister threshold temperatures may decrease more quickly than does the trend model for the mini-plates. Since the bulk of the data for the scale-up plates is from the AFIP–4 experiment (which does not reflect newer fabrication parameters being used) it is possible that different trend behaviors relative to fission density may be observed for scale-up plates to be blister threshold tested in the future.

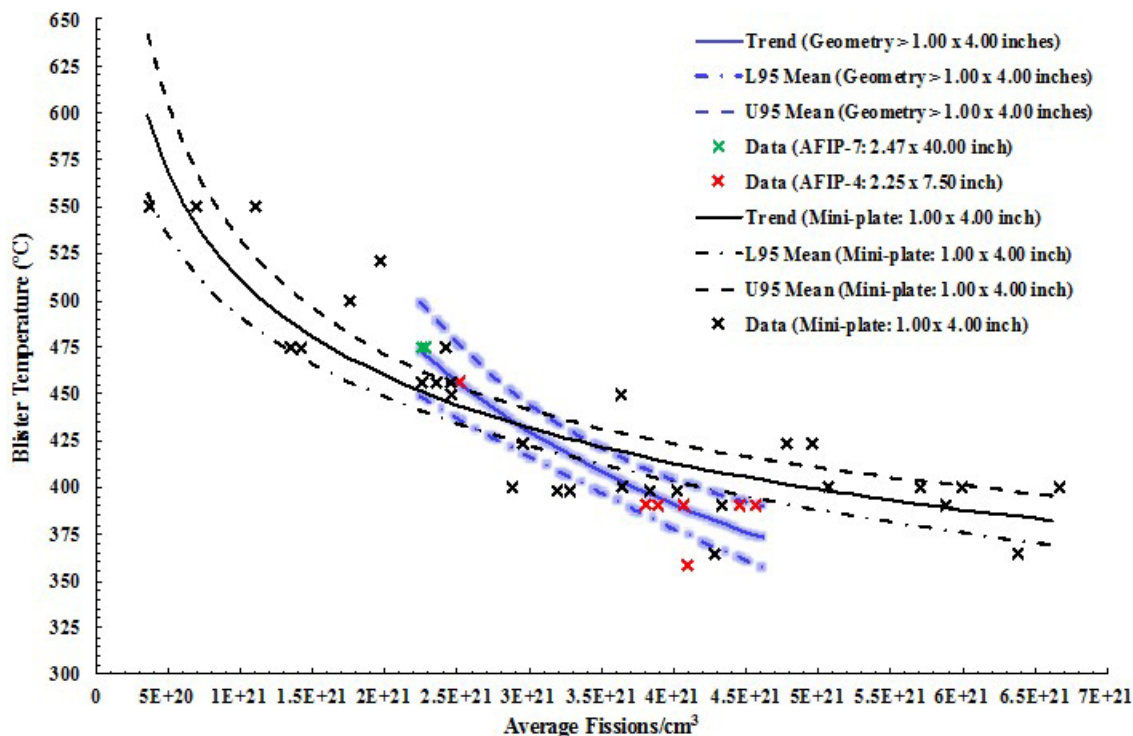


Figure 68. Monolithic blister threshold temperature data with separate trend models for mini-plates and larger plate geometries.

The section of plate 7ZH1 shown in Figure 55 indicate blisters traversing the width of the plate which is different than seen historically for monolithic fuel plates blister threshold tested to date. While the blisters are small, the fission density ($2.28\text{E}+21$ fissions/cm³) is also very low. Follow-on metallography of these blister anneal test plates is recommended to understand why these blisters appear different.

Plate 7ZH3 front and back blistered regions are shown Figure 56 and Figure 57 respectively and blister morphology for this plate is similar to previously blister threshold tested monolithic fuel plates where blisters formed locally in regions of highest burn-up, primarily along fuel edges.

Optical metallography examination of plate ZH2 and ZH4 indicated behavior expected for the lower fission density of this experiment. Several of the samples have small cracks originating at the cut end of the samples (Figure 40, Figure 41, Figure 42, Figure 44, and Figure 45). Due to the location and nature of the cracks it is assumed these are artifacts attributable to specimen preparation, a result of clamping the curved plate in order to perform the sub-sectioning. Sample 31 has significant cracking running the entire length of the sample.

No fission gas bubbles are visible within the fuel phase at these magnifications, indicating that no recrystallization of the fuel has occurred, even at the highest fission density examined, approximately $2.8\text{E}+21$ fissions/cm³, Figure 48. The fission gas is therefore assumed to still be predominantly contained within nano-bubbles dispersed in the fuel.¹³ Carbides can be seen dispersed throughout the fuel, which is typical for U-Mo alloys, but in this case they appear to be relatively small and evenly distributed, and they do not appear to have influenced fuel behavior at these fission densities.

Fuel/Zr/cladding interfaces all appear to be uniform and intact, essentially unchanged in appearance from the pre-irradiation microstructure.¹⁵ No significant interaction layers have formed during irradiation and no fission gas accumulation has occurred near the interfaces. Uncovered fuel foil edges appear to have behaved acceptably with minimal interaction layers forming between the fuel foil and cladding, and

no porosity formation evident. Oxide formation on the surface of the plates appears to be thin and uniform, on the order of 5-10 μm , in agreement with the eddy current measurements.

As shown in figures Figure 50-Figure 53, metallography of one of the samples prepared from plate ZH4 showed an unexpected inclusion phase near the surface of the fuel foil near and along the zirconium interlayer. The phase was variable and non-uniform, and appeared to contain microscopic fission gas bubbles that were not observed throughout the U-Mo fuel. The thickness of the zone varied up to approximately 120 μm and appeared to include multiple phases. The phases appeared to be hard and were likely present during fabrication, as evidenced by the zirconium diffusion barrier being deformed around the inclusion. It is important to note that this type of inclusion was only observed in one of the longitudinal samples, but it was several mm in length. The overall behavior of the plate was not negatively influenced by inclusion phase at the relatively low fission densities achieved in this experiment, however, at higher fission densities this phase could provide a pathway to the interconnection of fission gas bubbles or delamination of the interface. Pre-irradiation characterization suggests the inclusion phase is a uranium/carbide/nitride phase originating from the casting process. An image of an inclusion phase found during pre-irradiation characterization can be seen in Figure 69.¹⁶ It is important to identify and understand fabrication defects that impact fuel performance so that appropriate fabrication defect limits can be incorporated in fuel product specifications. Therefore, additional investigations are highly recommended to characterize the chemistry and structure of these inclusions, and to correlate the presence of these inclusions with defects that might have been observed the as-fabricated fuel, if possible.

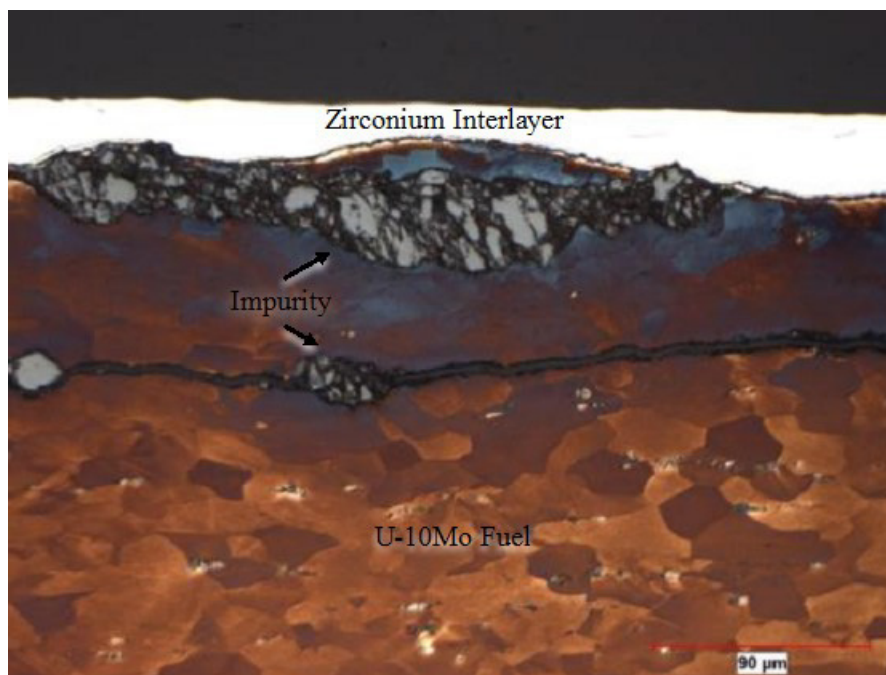


Figure 69. Pre-irradiation scanning electron image of inclusion phase similar to that observed during post irradiation examination.

6. CONCLUSIONS

The AFIP-7 monolithic fuel element was successfully irradiated under moderate conditions in the Advanced Test Reactor demonstrating the feasibility of the U-Mo fuel design in prototypic geometries involving curved, constrained fuel plates. The performance of the plates as determined through assessments of fuel swelling, blister threshold temperatures, and microstructural evolution was in line with previous monolithic tests and expectations for the fission densities achieved. A detailed swelling analysis was performed and the swelling behavior appears to be stable and predictable and is in good agreement with the previously published fuel swelling correlation developed by Kim and Hofman using historical data. The AFIP-7 experiment demonstrated that the fuel maintained mechanical integrity of the fuel meat, cladding, and interlayers, that the fuel maintained geometric stability necessary to ensure adequate coolability, and that the fuel swelling exhibited stable and predictable behavior.

7. REFERENCES

1. D. Wachs, *RERTR Fuel Development and Qualification Plan*, rev 5, INL external report INL/EXT-05-01017, 2011.
2. A. Robinson, "Irradiation Performance of U-Mo Alloy Based "Monolithic" Plate-Type Fuel - Design Selection," Web. doi:10.2172/968567, 2009.
3. N. Woolstenhulme*, D. Wachs and M. Meyer, "Design and Testing of Prototypic Elements Containing Monolithic Fuel," in *RERTR 2011 - 33rd INTERNATIONAL MEETING ON REDUCED ENRICHMENT FOR RESEARCH AND TEST REACTORS*, Santiago, Chile, 2011.
4. G. A. Moore, *AFIP-7 Fabrication Summary Report*, INL/LTD-12-26917, 2012.
5. W. Jones, "AFIP-7 Flow Test Summary", ECAR-3440, 2016.
6. N. Woolstenhulme, et. al., "Recent Accomplishments in the Irradiation Testing of Engineering-Scale Monolithic Fuel Specimens," in *RERTR 2012 – 34th INTERNATIONAL MEETING ON REDUCED ENRICHMENT FOR RESEARCH AND TEST REACTORS*, Warsaw, Poland, 2012.
7. D. M. Perez and J. W. Nielsen, *AFIP-7 Irradiation Summary Report*, INL External Report INL/EXT-12-25915, 2012.
8. S. Taylor, "AFIP-7 Ultrasonic Channel Gap Test Results", TEV-1280, 2012.
9. ASTM E376-11, "Standard Practice for Measuring Coating Thickness by Magnetic-Field or Eddy-Current (Electromagnetic) Testing Methods," ASTM International, West Conshohocken, PA, 2011.
10. MFC-USQ-2013-1272, "EJ-1402 GTRI Large Blister Anneal Furnace".
11. F.J. Rice, A.B. Robinson, M.K. Meyer, and N.J. Lybeck, *Preliminary Blister Anneal Testing Results for U-Mo Monolithic Fuel Plates*, INL/LTD-14-33608, 2014.
12. Y. S. Kim and G. Hofman, "Fission Product Induced Swelling of U-Mo Alloy Fuel," *Journal of Nuclear Materials* Vol. 419, 291-301, December 2011.
13. S. Van den Berghe, W. Van Renterghem, A. Leenaers, Transmission electron microscopy investigation of irradiated U-7 wt%Mo dispersion fuel, *Journal of Nuclear Materials*, Volume 375, Issue 3, 30 April 2008, Pages 340-346, ISSN 0022-3115.
14. J. C. Griess, H. C. Savage and J. L. English, *Effect of Heat Flux on the Corrosion of Aluminum by Water. Part IV*, ORNL-3, 1964.
15. J.F. Jue, D. Keiser, C. Breckenridge, T. Trowbridge, *AFIP-7 Characterization Report*, INL/LTD-14-34024, 2014.
16. D. L. Hammon and K. D. Clarke, *LANL Experience Rolling Zr-Clad LEU10Mo Foils for AFIP-7*, LANL Extnal Report LA-UR-11-02898, 2011.